

Contents lists available at ScienceDirect

Petroleum Science

journal homepage: www.keaipublishing.com/en/journals/petroleum-science



Original Paper

Study on S-wave velocity prediction in shale reservoirs based on explainable 2D-CNN under physical constraints



Zhi-Jun Li ^{a, b}, Shao-Gui Deng ^{a, b, *}, Yu-Zhen Hong ^{a, b}, Zhou-Tuo Wei ^{a, b}, Lian-Yun Cai ^c

- ^a State Key Laboratory of Deep Oil and Gas, China University of Petroleum (East China), Qingdao, 266580, Shandong, China
- b School of Geosciences, China University of Petroleum (East China), Qingdao, 266580, Shandong, China
- ^c Guangzhou Marine Geological Survey, China Geological Survey, Guangzhou, 511458, Guangdong, China

ARTICLE INFO

Article history: Received 1 October 2024 Received in revised form 2 March 2025 Accepted 27 April 2025 Available online 28 April 2025

Edited by Meng-Jiao Zhou

Keywords:
S-wave velocity prediction
Physically constrained 2D-CNN
Petrophysical model
Class activation mapping technique
Explainable results

ABSTRACT

The shear wave (S-wave) velocity is a critical rock elastic parameter in shale reservoirs, especially for evaluating shale fracability. To effectively supplement S-wave velocity under the condition of no actual measurement data, this paper proposes a physically-data driven method for the S-wave velocity prediction in shale reservoirs based on the class activation mapping (CAM) technique combined with a physically constrained two-dimensional Convolutional Neural Network (2D-CNN). High-sensitivity log curves related to S-wave velocity are selected as the basis from the data sensitivity analysis. Then, we establish a petrophysical model of complex multi-mineral components based on the petrophysical properties of porous medium and the Biot-Gassmann equation. This model can help reduce the dispersion effect and constrain the 2D-CNN. In deep learning, the 2D-CNN model is optimized using the Adam, and the class activation maps (CAMs) are obtained by replacing the fully connected layer with the global average pooling (GAP) layer, resulting in explainable results. The model is then applied to wells A, B1, and B2 in the southern Songliao Basin, China and compared with the unconstrained model and the petrophysical model. The results show higher prediction accuracy and generalization ability, as evidenced by correlation coefficients and relative errors of 0.98 and 2.14%, 0.97 and 2.35%, 0.96 and 2.89% in the three test wells, respectively. Finally, we present the defined C-factor as a means of evaluating the extent of concern regarding CAMs in regression problems. When the results of the petrophysical model are added to the 2D feature maps, the C-factor values are significantly increased, indicating that the focus of 2D-CNN can be significantly enhanced by incorporating the petrophysical model, thereby imposing physical constraints on the 2D-CNN. In addition, we establish the SHAP model, and the results of the petrophysical model have the highest average SHAP values across the three test wells. This helps to assist in proving the importance of constraints.

© 2025 The Authors. Publishing services by Elsevier B.V. on behalf of KeAi Communications Co. Ltd. This is an open access article under the CC BY license (http://creativecommons.org/licenses/by/4.0/).

1. Introduction

Fracability evaluation is an important basis for the efficient development of shale reservoirs (Li et al., 2020, 2022; Yang et al., 2021; Jiang et al., 2023). It is often determined using parameters such as Poisson's ratio, Young's modulus, and bulk modulus, and the key lies in the ability to obtain accurate S-wave velocity data. Meanwhile, the S-wave velocity also plays an important role in prestack seismic inversion and amplitude versus offset (AVO) analysis (Zhang et al., 2020; Yasin et al., 2021; Huang et al., 2023; Xu

* Corresponding author.

E-mail address: dengshg@upc.edu.cn (S.-G. Deng).

et al., 2024). However, the actual logging data frequently lacks S-wave velocity data, making its prediction crucial for practical purposes.

Currently, the prediction of S-wave velocity is mainly based on empirical formulas and petrophysical models. The empirical formulas usually use the P-wave velocity to establish a simple relationship equation. In recent years, many scholars have used conventional logging or core data to optimize or develop empirical models of various forms (Sohail and Hawkes, 2020; Yu et al., 2020; Zhang et al., 2020). Pickett (1963) proposed an empirical formula for S-wave velocity applicable to limestone based on a large collection of logging data; Han et al. (1986) analyzed the effect of clay content and porosity, and then they developed a linear regression model for S-wave velocity in sandstone under different

pressure conditions; Castagna et al. (1985) obtained an empirical formula for the relationship between different lithologies and S-wave velocity by analyzing experimental data; Vernik et al. (2018) analyzed the effect of total organic carbon (TOC) and then improved on the Greenberg-Castagna (GC) method, with prediction accuracy better than 3% error in all nine wells. The modeling process of the empirical formula method is relatively simple. The method is applicable to reservoirs with a single mineral component, requires researchers to have sufficient geological experience, and the calculation accuracy is often low. In addition, due to regional restrictions, the model varies greatly between different regions, and it is difficult to promote the application of the same model (Liu, 2021; Ye et al., 2022).

Petrophysical models describe the effect of microstructure on the overall properties of a rock. Classical petrophysical models of Swave velocity give the equations an obvious physical meaning by linking the microscopic features of rocks (e.g., porosity, pore structure) with macroscopic features (e.g., elastic modulus). Therefore, S-wave velocity prediction methods based on petrophysical models have become an important option. Xu and White (1995) analyzed the effect of the pore geometry, and based on the Gassmann equation and the Kuster-Toksöz (KT) model, they established the Xu-White model applicable to sandstone and mudstone; Yin et al. (2013, 2016) proposed an elastic modulus calculation method based on Biot theory and the Hudson model in tight sandstone with developed fractures and pores; Liu et al. (2022) established a S-wave velocity prediction method for tight sandstone reservoirs, considering the coexistence of polygonal pores and fractures. The petrophysical model has improved prediction accuracy compared to the empirical formula, and its application in conventional mud-sand stone and carbonate reservoirs has matured. However, due to the complexity of the mineral components in shale reservoirs, including clay minerals (illite and chlorite), carbonate minerals (calcite and ankerite), and quartz, feldspar, pyrite, and organic matters. The elastic modulus of various minerals varies greatly, which reduces the applicability of conventional petrophysical models. In addition, most of the existing models are applicable to the seismic exploration scale, and the accuracy of petrophysical modeling using logging data is low (Azadpour et al., 2020; Farouk et al., 2021).

In recent years, deep learning has achieved better application results in the field of logging (Ali et al., 2021; Bai and Tan, 2021; Liu et al., 2021; Y. Li et al., 2024), and the prediction of S-wave velocity using deep learning method shows a good development trend. Aiming at the interdependence of the upper and lower sections of the actual formation, some scholars have applied the long shortterm memory (LSTM) to solve the problem of the difficulty in predicting the S-wave velocity in complex reservoirs (Yang et al., 2019; Wang et al., 2020; Zhang et al., 2020). Logging data contains a large amount of formation information, but the relationship between the information is complicated and difficult to be fully utilized. Some scholars applied convolutional neural network (CNN) to automatically extract the features between logging data, and achieved better results (Zhang et al., 2022). Although CNN is good at extracting features related to S-wave velocity from logging data, it has limited ability to handle S-wave relationships at formation depth. Time series forecasting models, such as the LSTM and the gated recurrent unit (GRU), are effective in resolving long short-term dependencies in sequential data, but may not be as efficient as CNN in feature extraction. Therefore, some scholars have considered combining CNN with time series forecasting models (Wang and Cao, 2021; Wang et al., 2022; Zhang et al., 2022). The hybrid model not only feature the local perception characteristics but also has the long short-term memory function. This can also provide a useful reference for S-wave velocity prediction. It is

important to explore the application of high-precision deep learning methods in S-wave velocity prediction. However, these methods often lack the necessary transparency in the decisionmaking process. The "black box" characteristic of deep learning models may lead geophysicists to be skeptical of even highperformance models, because it is difficult for the model to give the appropriate decision basis for the predicted results (You et al., 2023). This hinders the practical application of deep learning models. Improving the explainability of deep learning methods is not only a technical challenge, but also a key to realizing their application in the geophysical field. In addition, the theoretical and practical application effects of the model can be promoted simultaneously by integrating petrophysical knowledge and deep learning methods. Therefore, when exploring the application of high-precision machine learning methods, in addition to pursuing the optimization of algorithm performance, it is equally important to enhance the physical constraints and explainability.

Therefore, we propose a physically-data driven method for the S-wave velocity prediction in this paper, using the shale reservoir data in the southern Songliao Basin, China, as a case study. This method combines the class activation mapping (CAM) technique with physically constrained 2D-CNN. Firstly, we perform a sensitivity analysis of S-wave velocity, and data with high-sensitivity are used as the basis. Secondly, based on analyzing the mineral components, we use the petrophysical properties of porous medium and the Biot-Gassmann equation to establish a model with clear physical significance. Subsequently, its results are combined with the fundamental logging data to realize the constraints on the 2D-CNN. Finally, we develop the CAM technique to tackle the inherent black-box problem and propose a defined C-factor for evaluating the level of concern. This can help to explain the model's results and constraint behaviors, thereby improving reliability. In addition, we built a summary plot based on SHAP, it can assist in proving the importance of constraints.

2. Data collection and analysis

2.1. Background

Songliao Basin is a large Mesozoic-Cenozoic basin in eastern China, located at the junction of Liaoning, Jilin, and Heilongjiang provinces. Influenced by tectonic movements and sedimentations, the basin has formed abundant oil and gas resources (Liu et al., 2019; Zhang et al., 2020; Li et al., 2024). The data for this study is from the Qing1 member of the Qingshankou Formation. The shale in the area has proven to be well developed during exploration (Bai et al., 2022; Wang et al., 2023; Zhang et al., 2023). Obtaining an accurate S-wave is followed by fracability evaluation. This is important for mining efficiency and capacity prediction. However, the high cost of S-wave logging (e.g., dipole acoustic logging) has resulted in a lack of S-wave information. Therefore, it is important to establish a stable and accurate S-wave velocity prediction model based on limited information.

This paper selects three wells with comprehensive data as training and testing samples. Well A spans a depth range of X288 to X189 m with a sampling interval of 0.1 m, consisting of 9010 sets of data. We use the section of the well depth range from X288 to X079 m, which contains 7910 sets of data, as the training set for cross-validation, and the section from X079 to X189 m, which contains 1100 sets of data, as the test set. The distribution of logging parameters for the training set is shown in Fig. 1.

Well B1 spans a depth range of X359 to X455 m with a sampling interval of 0.1 m, containing 960 sets of data for testing. Additionally, well B2 spans a depth range of X491 to X601 m with a sampling interval of 0.125 m, providing 880 sets of data for testing. Fig. 2

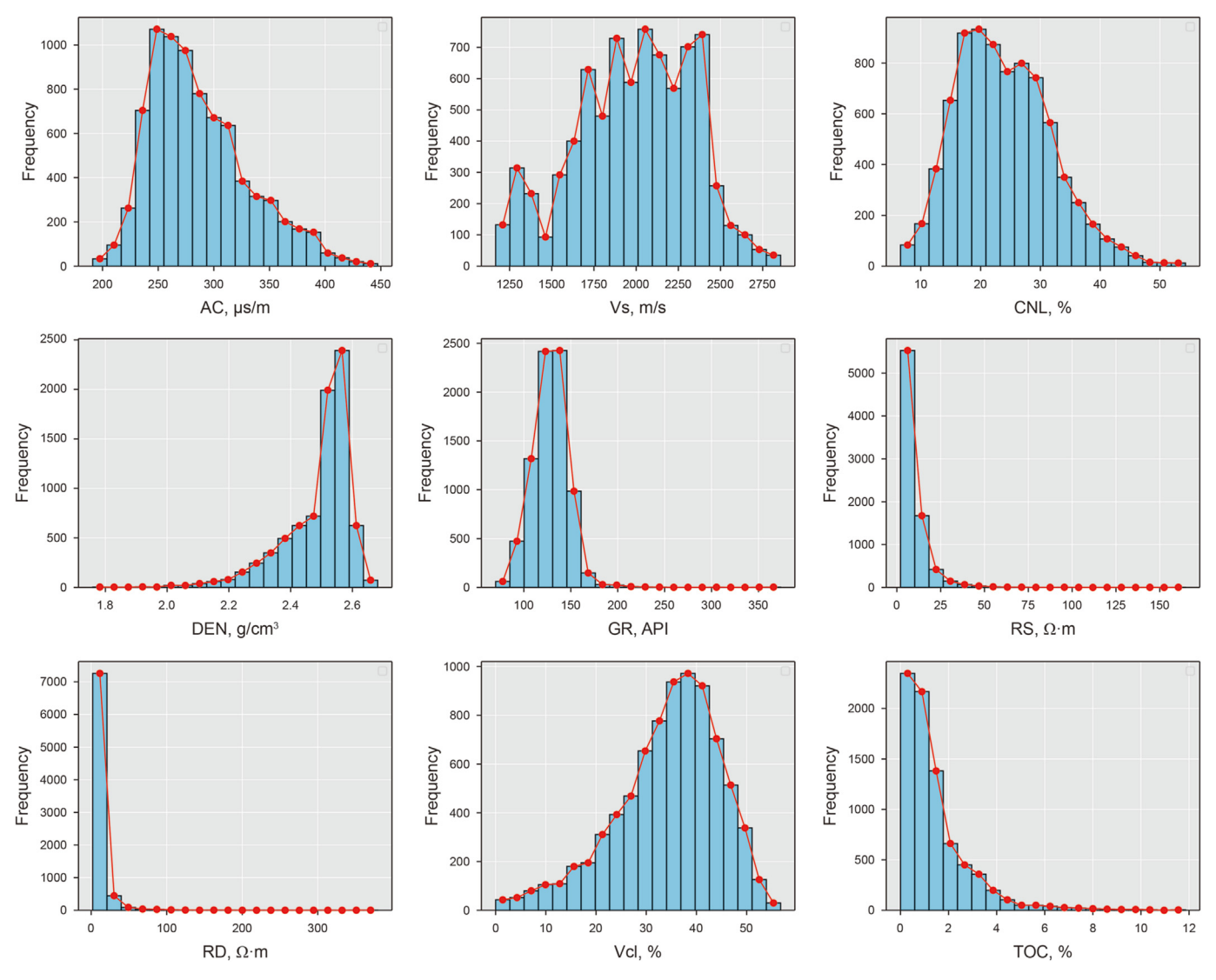


Fig. 1. Parameters distribution of the training set.

displays the distribution location of the three wells in the study area. There are three reasons for this division. Firstly, the data from well A is relatively abundant, and after training the model with the data from the upper section, the data from the lower section can verify the model's curve-completion ability. Secondly, well B1 can verify the accuracy of the model's prediction of blind wells. Finally, the location of well B2 is relatively far from well A, and the prediction results can further reflect the model's generalization ability. This evaluation will further determine the suitability of the model for broader implementation in the study area.

2.2. Relationship between logging data and S-wave velocity

We establish the cross plots of acoustic (AC), compensated neutron log (CNL), density (DEN), natural gamma ray (GR), deep and shallow lateral resistivity (RD, RS), spontaneous potential (SP), caliper (CAL), clay content (Vcl), and TOC with S-wave velocity, respectively, to analyze the relationship between S-wave velocity and logging data. Fig. 3 displays the cross plots of logging data and S-wave velocity in the southern Songliao Basin.

The AC is commonly used to determine rock porosity and calculate mineral content, and there is a very strong linear negative correlation with S-wave velocity (Fig. 3(a)). In general, P-wave

velocity and S-wave velocity are affected by factors such as rock mass stiffness and density. As stiffness and density increase, the acoustic wave propagation velocity also increases. The empirical model of S-wave velocity is usually used with AC data, but in practice, the method's generalization ability is weak.

The CNL is used to determine formation porosity, a measure of the amount of hydrogen contained in the rock. There is a strong negative correlation with the S-wave velocity (Fig. 3(b)). In general, as formation porosity and hydrogen atom content increase, so does the liquid medium, leading to a decrease in S-wave velocity due to the difficulty of S-wave propagation through the liquid. In addition, high porosity formation has low density and elastic modulus, which leads to lower S-wave velocity.

The DEN is used to determine the porosity of formation, lithology identification, etc. DEN data are important in S-wave velocity prediction, which is a key parameter in the calculation of bulk modulus and shear modulus. It has a linear and positive correlation with S-wave velocity (Fig. 3(c)). The density of the rock is generally affected by the rock mineral fraction and pore space or fluid. With the increase in density, the skeleton content of the rock increases, and the rock mass stiffness will increase, which leads to an increase in transverse wave velocity.

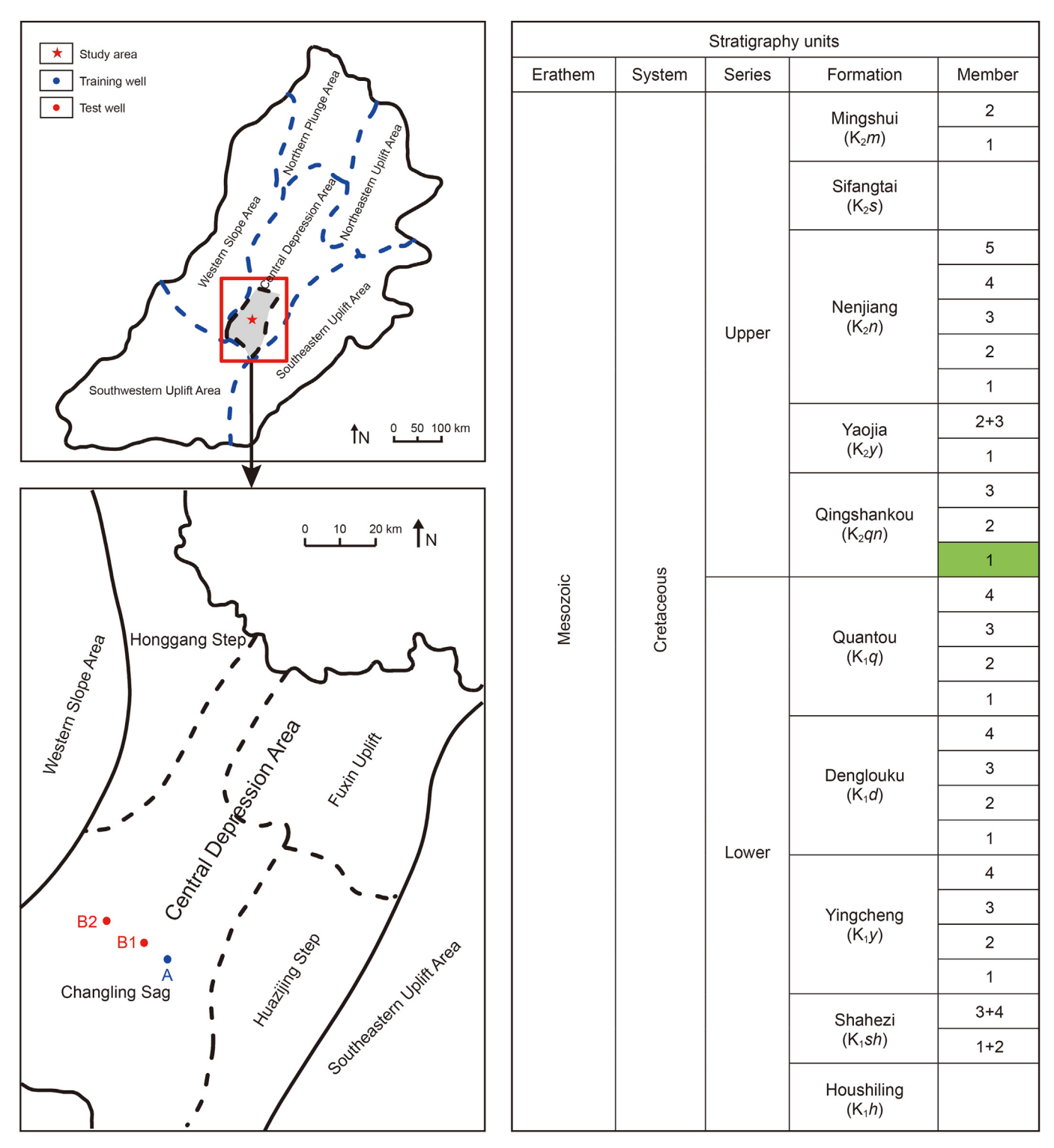


Fig. 2. The location map and the stratigraphic column for three wells in the study area.

The GR log measures the intensity of radioactive elements in the formation. It reflects the clay mineral content and judges the lithology of the formation. It is negatively correlated with the S-wave velocity (Fig. 3(d)). As the GR rises, the clay mineral content increases, thus affecting the S-wave velocity.

The RD/RS log can reflect the change in formation resistivity more realistically. They can quickly and intuitively determine the oil and water layers, and they have a better exponential

relationship with the S-wave velocity (Fig. 3(e) and (f)). Formation resistivity is affected by porosity and pore structure; when the pore connectivity is good, it will affect the S-wave propagation path and reduce the velocity. At this time, the fluid can flow freely in the pore space, which leads to lower resistivity values.

The SP log measures the potential generated by the electrochemistry of the formation. For weakly conductive formations, there is a negative correlation with S-wave velocity (Fig. 3(g)). This

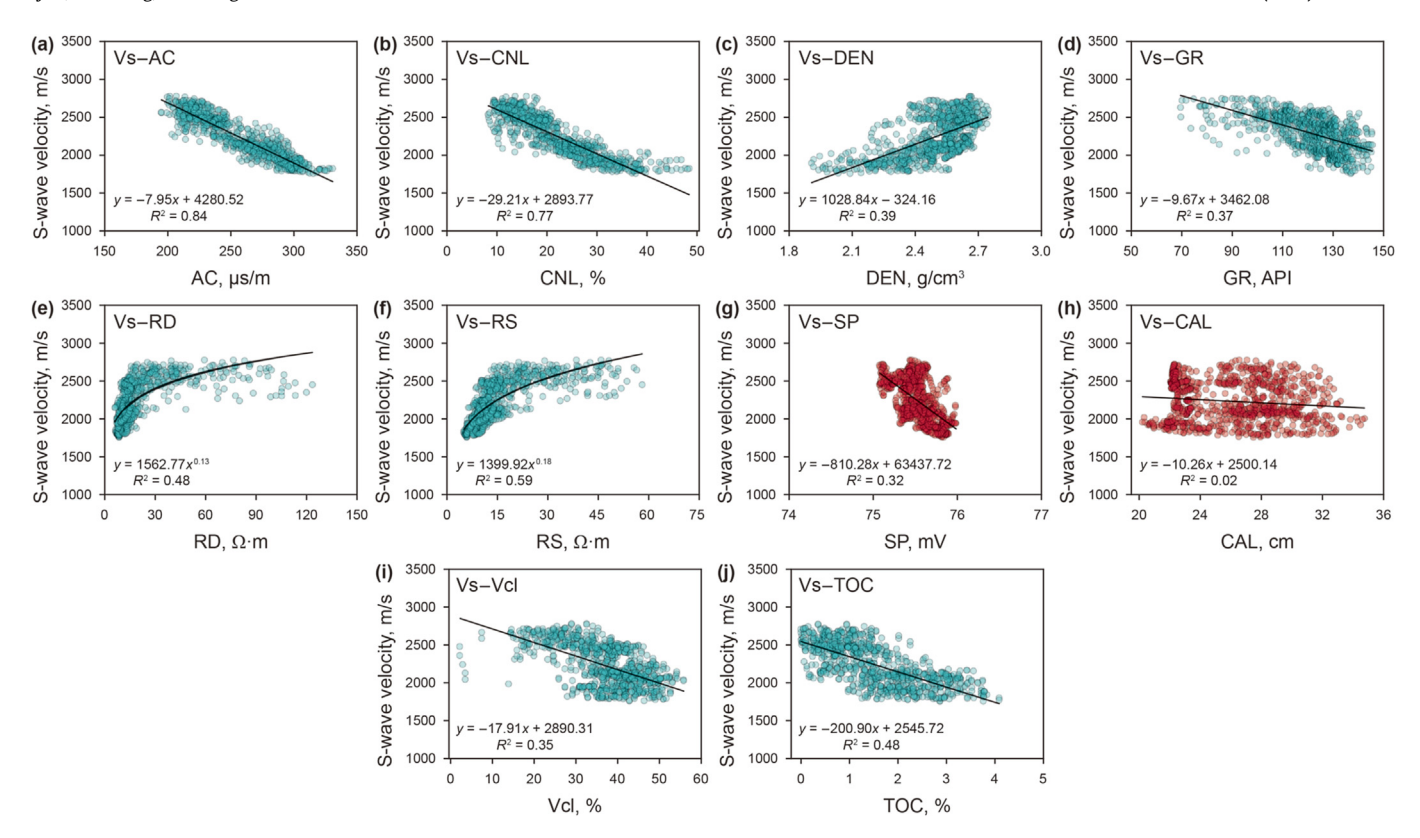


Fig. 3. The cross plots of logging data and S-wave velocity.

is due to the fact that less SP is generated when conductivity is low. And insulating rocks generally have higher elastic properties that help S-wave propagate through the formation.

The CAL log is often used as auxiliary information. It is used in conjunction with the GR and SP to synthesize stratigraphic profiles and identify lithology. It has no correlation with S-wave velocity (Fig. 3(h)).

By analyzing the elemental logging data, the clay content and TOC can be obtained. Among them, the clay content is mainly influenced by clay minerals such as illite and chlorite, which have small particle diameters. It is negatively correlated with the S-wave velocity (Fig. 3(i)). When the rock contains a high clay content, its pore space will be filled by clay particles, and the cementing effect of clay will slow down the propagation speed of the S-wave.

The TOC refers to the organic matter content (e.g., hydrocarbons) in the formation and is negatively correlated with S-wave velocity (Fig. 3(j)). On the one hand, organic matter has a lower density and elastic modulus, which reduces the elastic properties of the formation. On the other hand, the pore structure and composition of organic matter also affect the pore distribution, pore connectivity, and the size of the pore space of the formation. Thus, it affects the pore fluid saturation and further affects the propagation velocity of S-waves in the formation. When TOC data are lacking in the study area, the Δ logR method can be utilized to derive the TOC value in the shale formation (Khoshnoodkia et al., 2011).

In summary, based on the sensitivity analysis of the S-wave velocity in this study area, the AC, CNL, DEN, GR, RD/RS, clay content, and TOC are selected as the base data for the model.

2.3. Mineral component analysis

Based on elemental logging data, it is determined that the study area contains mainly clay minerals (illite and chlorite), carbonate

minerals (calcite and ankerite), quartz, feldspar, and pyrite (Fig. 4). In the test section of well A, carbonate minerals range from 0% to 46.2% with a mean of 7.8% (calcite content 4.5%, ankerite content 3.3%); clay minerals range from 0% to 67.6 % with a mean of 29.2%; and quartz, feldspar, and pyrite totaling range from 30% to 91.3% with a mean of 63.0% (quartz content 32.0%, K-feldspar content 5.0%, N-feldspar content 25.7%, and pyrite content 0.3%). In well B1, carbonate minerals range from 0% to 51.0% with a mean of 9.8% (calcite content 5.6%, ankerite content 4.2%); clay minerals range from 0% to 55.8% with a mean of 36.9%; quartz, feldspar, and pyrite totaling range from 33.9% to 77.3% with a mean of 53.3% (quartz content 24.7%, K-feldspar content 4.2%, N-feldspar content 23.8%, and pyrite content 0.6%). In well B2, carbonate minerals range from 0% to 44.5% with a mean of 7.9% (calcite content 4.7%, ankerite content 3.2%); clay minerals range from 0.1% to 64.7% with a mean of 36.2%; and quartz, feldspar, and pyrite totaling range from 31.9% to 88.7% with a mean of 55.9% (quartz content 26.6%, K-feldspar content 4.3%, N-feldspar content 24.3%, and pyrite content 0.7%).

Through the above analysis, we found that the mineral compositions of these three well sections are similar, but the components are more complex. This complexity is not only reflected in the diversity of mineral species, but also in the content ratio between various minerals, which brings challenge to the S-wave velocity prediction. Therefore, we need to consider how to utilize the mineral component data to establish a petrophysical model applicable to the study area, which provides an important foundation for accurate S-wave velocity prediction.

3. Model overview

3.1. Convolutional neural network

Compared with the 1D-CNN, the 2D-CNN can effectively capture the local patterns and global relationships of the feature maps. It

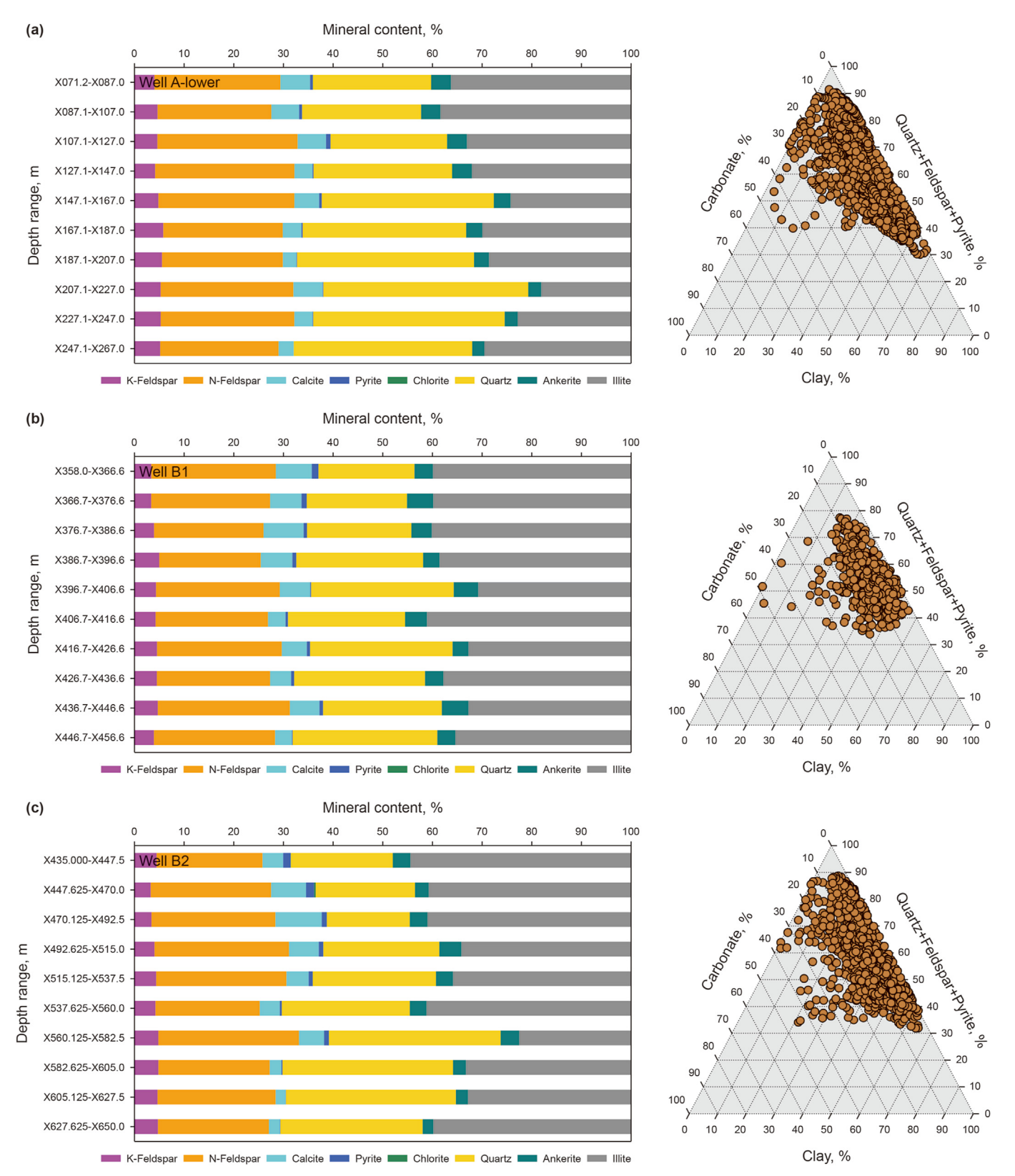


Fig. 4. Mineral composition of three test sections.

can extract important information about the spatial location by performing convolutional operations in the two dimensions of height and width (Yildirim et al., 2019; Zhao et al., 2019, 2021). Its biggest advantage is that the convolutional layer is the core. The

convolution operation can extract effective features from the data in the previous layer, and the subsequent convolution operation can obtain more complex feature information from the combination of these effective features. The convolutional layer usually contains many feature maps, each of which consists of multiple neurons arranged in a matrix, and neurons in the same feature map share weights. In addition to this property of weight sharing, the convolutional kernel allows for the extraction of local features from the feature map through local connectivity. The obvious benefit of these two qualities is that they minimize the network's layer-to-layer connections, which dramatically reduces model parameters and increases training efficiency while lowering the risk of overfitting. At the beginning of training, the convolution kernel is usually initialized in the form of a matrix of random decimals, and the convolution kernel will learn to get the appropriate weights. The following is the convolution operation:

$$\mathbf{y}_{ij} = \sum_{m=0}^{M-1} \sum_{n=0}^{N-1} \mathbf{w}_{mn} \mathbf{x}_{i+m,j+n} + \mathbf{b}$$
 (1)

where \mathbf{x} is the input data; M and N are the width and height of the convolution kernel, respectively; \mathbf{w} is the corresponding weight matrix; \mathbf{b} is the bias; \mathbf{y} is the result of the convolution operation.

To handle the nonlinear problem more effectively, an activation function is applied after the convolution operation, and the result is utilized as the convolution layer's output:

$$\mathbf{x} = f(\mathbf{y}), (f \supseteq \{\text{ReLU}, \text{tanh}, \text{Sigmoid}, \text{etc.}\})$$
 (2)

where f is the activation function, there are various forms of activation function that can be selected according to the actual needs; \mathbf{x} is the output of the activation function.

In order to quantify the difference between the predicted values and the true values, the mean square error (MSE) function is chosen. The formula is as follows:

$$l = \frac{1}{n} \sum_{i=1}^{n} (y_i - t_i)^2$$
 (3)

where n is the number of samples; y_i is the predicted values; t_i is the true values.

3.2. Class activation map

The CAM is a visualization method used to explain the decision-making process of the CNN. By correlating the last layer of convolutional feature maps in the network with the prediction values, a heat map is generated to visualize the degree of attention of the CNN to the input feature map. When the value of a region in the heat map is higher, it indicates that the model pays more attention to that region (Zhou et al., 2016; Selvaraju et al., 2017).

The CAMs generation process is based on the global average pooling (GAP) layer and linear weight mapping. GAP is used in the last layer of the feature map, and the formula is as follows:

$$\mathbf{G}_n = \frac{\sum\limits_{i=1}^{x}\sum\limits_{j=1}^{y}\mathbf{a}_{ij}^n}{xv} \tag{4}$$

where G_n is the average value of the nth channel; x and y are the length and height of the last layer of the feature map, respectively; \mathbf{a}^n_{ij} is the value with coordinates (i, j) in the nth channel.

Further, the formula that generates the CAMs is as follows:

$$\mathbf{M}(x,y) = \sum_{i=1}^{n} \mathbf{w}_{i} \mathbf{f}_{i}(x,y)$$
 (5)

where (x, y) is the size of the CAMs and the last layer of feature map; \mathbf{w}_n is the corresponding weight obtained after GAP of the nth channel; \mathbf{f}_i is the feature map of the ith channel.

In the training phase, the feature maps are converted into feature vectors of the prediction values by applying GAP to the last layer of feature maps. Then, the weights of the prediction values are obtained by applying linear weight mapping on the feature vectors. In the testing phase, forward propagation is computed to the input feature maps. Then the weights of the prediction values are multiplied with the corresponding last layer of feature maps, and the results are summed to obtain the CAMs. The model structure is shown in Fig. 5. From the figure, it can be seen that GAP layer replaces the fully connected (FC) layer, which reduces the number of parameters and prevents the model from overfitting.

It is worth noting that this model does not use a pooling layer after the convolution operation. On the one hand, the nature of the pooling layer is to reduce the model parameters by converting large feature maps into small ones. However, the conventional log curves converted into 2D feature maps has less data, and the model does not need to reduce the dimensionality of the feature maps; on the other hand, the pooling layer has translational invariance. The introduction of the pooling layer causes the CNN to be insensitive to the position in the input feature map. This makes the model lose spatial information and hinders the explainability of the parameters.

3.3. Petrophysical modeling of S-wave velocity

The relationship between P-wave and S-wave velocity and shear modulus, bulk modulus, and density of the rock is as follows:

(3)
$$\begin{cases} V_{\rm p} = \sqrt{\frac{K + \frac{4}{3}\mu}{\rho}} \\ V_{\rm s} = \sqrt{\frac{\mu}{\rho}} \end{cases}$$
 (6)

where $V_{\rm p}$ and $V_{\rm s}$ are the P-wave/S-wave velocity, respectively, km/s; ρ is the density, g/cm³; K is the bulk modulus, GPa; μ is the shear modulus. GPa.

In shale reservoirs, the mineral components and pore structure of rocks are complex. The elastic modulus gap between fluids within the pore and skeletons is obvious. Therefore, the P-wave velocity and S-wave velocity are difficult to calculate by Eq. (6). It is necessary to establish an equivalent medium model for the mineral properties and different pore fluids. The Biot-Gassmann theory reveals the elastic parameter relationship between the solid and fluid phases in the saturated fluid pore medium at low frequency (Shao et al., 2009). The formula is as follows:

(4)
$$\begin{cases} K_{\rm d} = (1-B)K_{\rm m} \\ \mu_{\rm d} = (1-B)\mu_{\rm m} \\ \mu = \mu_{\rm d} \\ K = K_{\rm d} + B^2M \\ \frac{1}{M} = \frac{B-\varphi}{K_{\rm m}} + \frac{\varphi}{K_{\rm fl}} \end{cases}$$
 (7)

where K and μ are the bulk modulus and shear modulus in the formation, GPa; K_d and μ_d are the bulk modulus and shear modulus of dry rock, GPa; K_m and μ_m are the bulk modulus and shear modulus of the rock skeleton, GPa; B is the Biot coefficient, a decimal; ϕ is the porosity of the formation, a decimal; M is the pressure

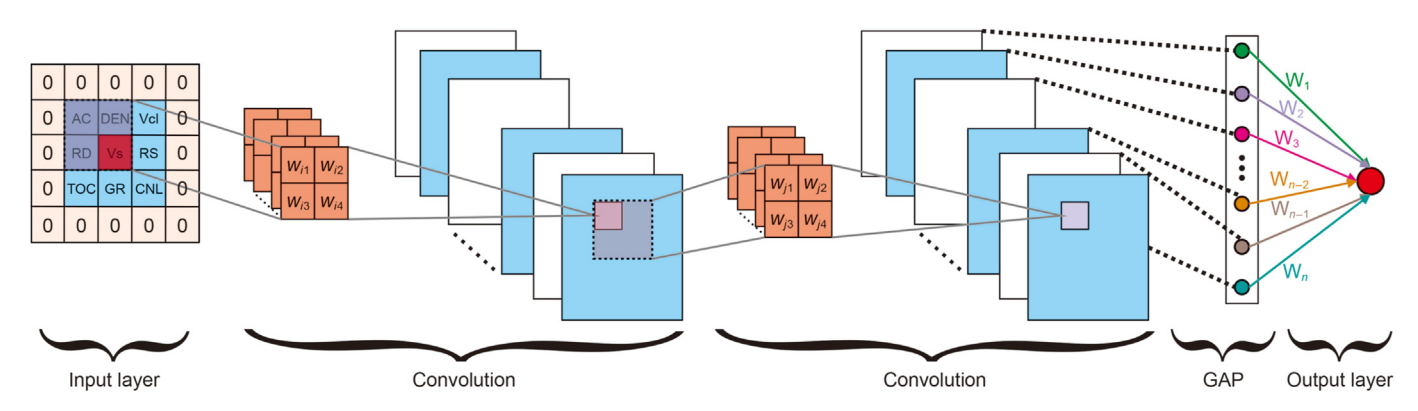


Fig. 5. Schematic diagram of model structure.

that needs to be applied to the fluid to increase the fluid content by a unit volume during equal volume macro-strain, MPa; $K_{\rm fl}$ is the bulk modulus of the fluid in the formation, GPa.

For shale oil reservoirs, the fluids in the formation are mainly irreducible water and oil. The equivalent volume model is calculated as follows:

$$\frac{1}{K_{\rm fl}} = \frac{S_{\rm w}}{K_{\rm w}} + \frac{1 - S_{\rm w}}{K_{\rm o}} \tag{8}$$

where K_W and K_O are the bulk modulus of water and oil, respectively, GPa; S_W is the water saturation, a decimal.

In this paper, the Voigt-Reuss-Hill (VRH) model is used to solve the skeletal equivalent bulk modulus and shear modulus of complex minerals. Firstly, Voigt gave the upper limit of the equivalent elastic modulus of the mixed medium. The formula is as follows:

$$\begin{cases} K_{\mathbf{v}} = \sum_{i=1}^{n} f_i K_i \\ \mu_{\mathbf{v}} = \sum_{i=1}^{n} f_i \mu_i \end{cases}$$
 (9)

where n is the mineral species in the rock; K_v and μ_v are the upper limits of the equivalent bulk modulus and shear modulus of the mixed medium, respectively, GPa; K_i and μ_i are the bulk modulus and shear modulus of the ith mineral component, respectively, GPa; f_i is the volume content of the ith mineral component, a decimal.

Next, Reuss gave lower limits for the equivalent elastic modulus of a mixed medium. The formula is as follows:

$$\begin{cases} \frac{1}{K_{\rm r}} = \sum_{i=1}^{n} f_{i} \frac{1}{K_{i}} \\ \frac{1}{\mu_{\rm r}} = \sum_{i=1}^{n} f_{i} \frac{1}{\mu_{i}} \end{cases}$$
(10)

where $K_{\rm r}$ and $\mu_{\rm r}$ are the lower limits of the equivalent bulk modulus and shear modulus of the mixed medium, respectively, GPa.

Finally, Hill arithmetically averaged the results of the upper and lower calculations. The equivalent bulk modulus and shear modulus of the rock skeleton are obtained. The formula is as follows:

$$\begin{cases} K_{\rm m} = \frac{K_{\rm r} + K_{\rm v}}{2} \\ \mu_{\rm m} = \frac{\mu_{\rm r} + \mu_{\rm v}}{2} \end{cases}$$
 (11)

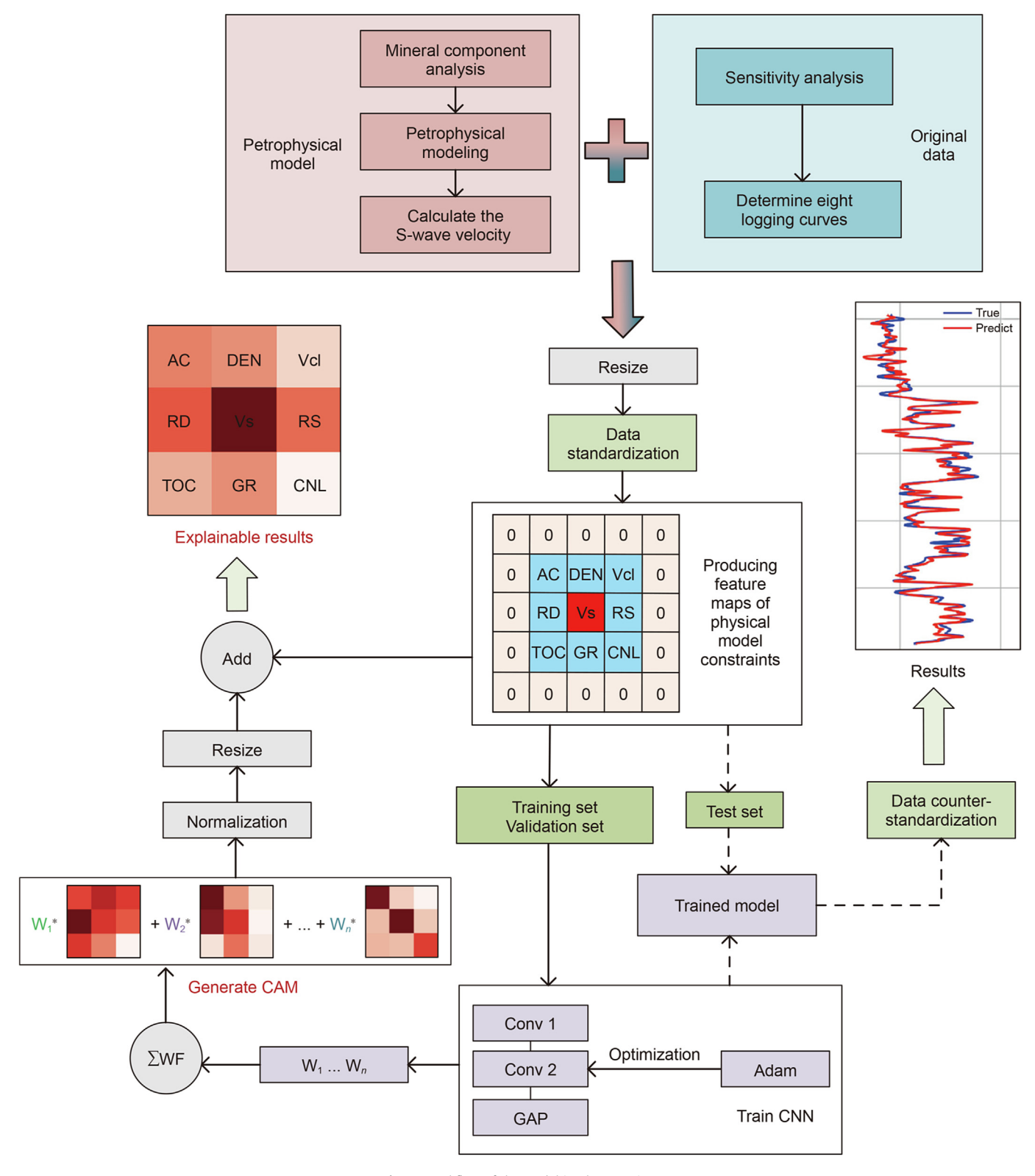
The conversion equations for the P-wave/S-wave velocity to the equivalent bulk modulus and shear modulus are obtained from Eqs. (6)-(11):

$$\begin{cases} V_{p} = \sqrt{\frac{(1-B)\left(K_{m} + \frac{4}{3}\mu_{m}\right) + \frac{B^{2}K_{m}K_{fl}}{BK_{fl} + \left(K_{m} - K_{fl}\right)\phi}} \\ V_{s} = \sqrt{\frac{(1-B)\mu_{m}}{\rho}} \end{cases}$$
(12)

In Eq. (12), the measured AC can be used to calculate the S-velocity. This method has the following advantages over petrophysical model based on Xu-White: (1) When using Xu-White model to calculate the $V_{\rm p}$ and $V_{\rm s}$, the wave velocity parameter of the mixed mineral rock skeleton is needed. To obtain accurate parameter, it is necessary to use the core samples of the study area to carry out experimental measurements. In this paper, the multi-mineral model does not need the parameters of wave velocity and pore shape of the mixed mineral rock skeleton, so it does not rely on the experimental data of the core, which can reduce the experimental measurements and statistical analysis, and save the cost of the test and time. (2) This method calculates the elastic modulus based on the rock skeleton and fluid components, and after obtaining the equivalent elastic modulus of the formation, the S-wave velocity can be calculated. The steps have a clear physical meaning and satisfy the conditions for constraining the deep learning model. (3) Since the AC is used as a constraint condition, the S-wave velocity can be calculated accurately as long as the solution of mineral components is reasonable, this method has high stability and accuracy.

3.4. Physically-data driven method

Fig. 6 shows the workflow for the physically-data driven model. Based on the elemental logging data, the mineral component of the well is determined. The equivalent elastic modulus of the formation is obtained by using the VRH boundary average model, and the S-wave velocity is obtained by calculating the Biot-Gassmann equation. At the same time, sensitivity analysis is done on the logging data, such as AC, CNL, DEN, and S-wave velocity, eight kinds of logging data with high-sensitivity are identified. Then, it is converted into a single-channel 2D feature map by combining the calculated values of S-wave velocity (determined by petrophysical modeling). Next, the data is normalized and divided into training and test sets. The training sets are input to the pre-trained CNN to obtain the feature representation of the input data in the model



 $\textbf{Fig. 6.} \ \ \textbf{Workflow of the model implementation}.$

through forward propagation. The weights of the model are weighted linearly with the feature map of the last convolutional layer, and then the class activation map is obtained. The CAMs are normalized and up-sampled to the same size as the input feature

map through the inverse convolution operation. In turn, the visualization is achieved by overlaying with the original feature map.

The advantages of this method: (1) The 2D feature map can be obtained by adding the S-wave velocity (determined by petrophysical modeling), and more important information can be

extracted by performing convolutional operations in the two dimensions of height and width, which helps to improve the prediction accuracy. (2) The petrophysical model portrays the physical relationship between the S-wave velocity and the petrophysical features, which has clear physical significance. After physical constraints, it helps to improve the correlation between the prediction results and the real values, so that the trend of the prediction results is more consistent with the real values. (3) The CAMs can explain how much attention the CNN pays to each location of the input data. This helps to understand the basis of the network's decisions.

4. S-wave velocity prediction

4.1. Petrophysical model

Elemental logging data show that the rock minerals in the study well section mainly include illite, quartz, calcite, pyrite, feldspar, ankerite, etc., and the mineral composition is complex. Due to the large differences in the elastic modulus parameters of different minerals, see Table 1.

The model of Section 3.3 is applied to develop a petrophysical model of the S-wave velocity with the multi-mineral component. In Eq. (12), the value of the Biot coefficient is derived from the measured AC data to obtain the S-wave velocity. Due to the small porosity in the mud shale section, in practical application, the $(K_{\rm m}-K_{\rm fl})\,\phi$ in the denominator of the quadratic term is regarded as 0 for the convenience of calculation, and Eq. (12) is changed to the following equation:

$$V_{\rm s} = \sqrt{\frac{3\left(\rho V_{\rm p}^2 - K_{\rm m}\right)}{4\rho}}\tag{13}$$

The calculated value of S-wave velocity obtained with Eq. (13) in three well sections is plotted against the measured value, as shown in Fig. 7. It can be seen that the calculated and measured values are relatively good near the diagonal with a slope of 1, which provides an important guarantee for subsequent processing.

The model has a clearer physical meaning by idealizing the actual formation and obtaining the equivalent elastic modulus based on the rock skeleton and fluid components. Although the Biot coefficient obtained by using the AC improves the limitations of the Gassmann equation applicable under high-frequency conditions to a certain extent, the actual results show that the model is still a macroscopic reflection of the S-wave velocity in the study area. It is difficult to depict the diversity of geological conditions in shale formation, such as strong anisotropy and non-homogeneity. Therefore, a physically constrained 2D-CNN is proposed to use the physical model as a macroscopic control, and the CNN is utilized for fine portrayal. The $V_{\rm S}$ calculated by Eq. (13) is combined with the basic data as the model input to constrain the CNN.

4.2. Data processing

Eight types of logging data with high correlation to S-wave velocity are selected as the basis, including AC, CNL, DEB, GR, RD, clay content, and TOC. The above computed $V_{\rm S}$ is added to constrain the model, which in turn converts these nine parameters into 3×3 two-dimensional data as inputs to the CNN model. This study is constructed using the Pytorch framework and the Python programming language.

Since the magnitude of the values is different between the logging data, if the original data values are used directly, then the degree of influence on the S-wave velocity will be different among the logging data. This will lead to slow convergence or even non-convergence. Therefore, we need to standardize the original data. The standardization formula is:

$$x_{ij_s} = \frac{\left(x_{ij} - x_{i_avg}\right)}{\sqrt{\frac{1}{n} \sum_{k=1}^{n} \left(x_{ik} - x_{i_avg}\right)^2}}$$
(14)

where x_{ij_S} is the normalized data; x_{ij} is the pre-normalized data; x_{i_avg} is the mean value of each log curve; $x_{i_avg} = (GR_{avg}, SP_{avg}, RD_{avg}, RS_{avg}, AC_{avg}, CNL_{avg}, DEN_{avg})$; n is the number of samples.

4.3. Model architecture design

In this experiment, the abstract feature extracted by the convolutional layers is the relationship between the input data and the S-wave velocity. The model is trained by means of supervised learning, and to solve the nonlinearity problem, the ReLU activation functions are added after each convolutional layer:

$$f(\mathbf{x}) = \max(0, \mathbf{x}) \tag{15}$$

The use of the ReLU function can effectively prevent the gradient from disappearing, preventing the model from overfitting. Compared with the sigmoid function and tanh function, its derivatives are better obtained, and in the process of constantly updating the parameters, due to its simple form, it has a faster training speed.

The Adam algorithm is employed in the model for optimization purposes. By incorporating bias correction, the learning rate has a definite range in each iteration. This enhances the smoothness of the gradient descent operation, ensures accuracy, and facilitates more effective updates to the network weights (Yi et al., 2020). The updating operation is as follows:

$$\mathbf{v}_t = \beta_1 \mathbf{v}_{t-1} + (1 - \beta_1) \mathbf{\varphi}_t \tag{16}$$

 Table 1

 Elastic properties of mineral components (Passey et al., 1990).

Minerals		Bulk modulus, GPa	Shear modulus, GPa	Density, g/cm ³
Clay minerals	Illite Chlorite	25	9	2.55
Carbonate minerals	Ankerite	95	45	2.87
	Calcite	77	32	2.71
Others	Quartz	38	44	2.65
	Feldspar	18	15	2.62
	Pyrite	144	129	4.81
Fluids	Oil	0.57	0	0.7
	Water	2.25	0	1.04

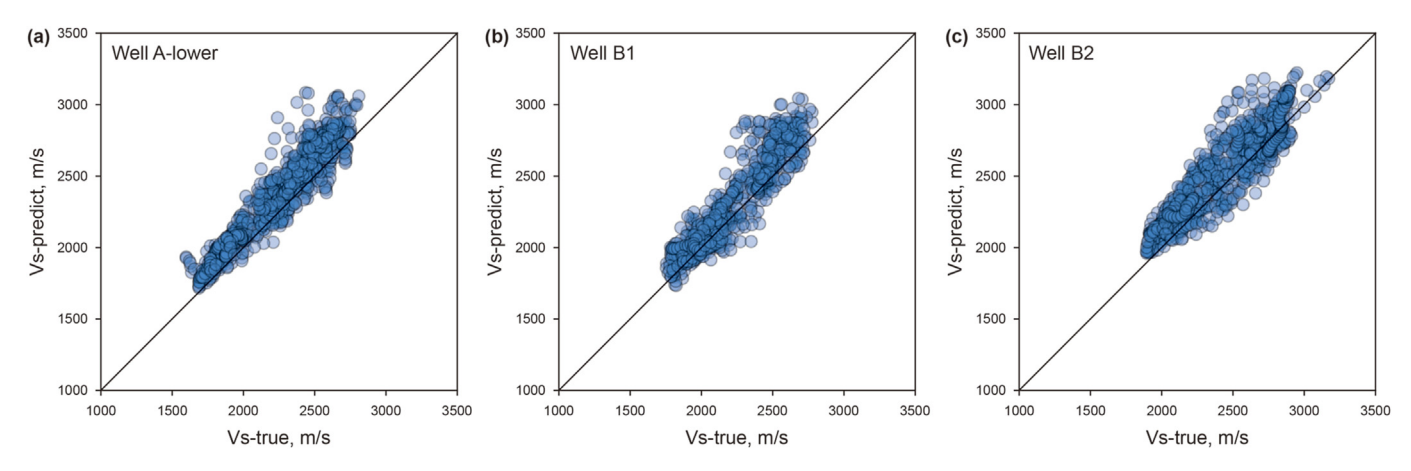


Fig. 7. Petrophysical modeling values versus measured values.

$$\mathbf{s}_{t} = \beta_{2} \mathbf{s}_{t-1} + (1 - \beta_{2}) \mathbf{\phi_{t}}^{2} \tag{17}$$

where \mathbf{v}_t and \mathbf{s}_t are the first-order and second-order momentum items of the tth iteration, respectively; β_1 and β_2 are the exponential decay rates of the first-order and second-order moment estimates, respectively; β_1 and β_2 are set to 0.5 in this paper; φ_t is the value of the cross-entropy gradient at the tth iteration.

In order to eliminate the initialization bias, the bias correction is applied to \mathbf{v}_t and \mathbf{s}_t , respectively:

$$\mathbf{v}_t' = \frac{\mathbf{v}_t}{1 - \beta_1^t} \tag{18}$$

$$\mathbf{s}_t' = \frac{\mathbf{s}_t}{1 - \beta_2^t} \tag{19}$$

Finally, the parameter update expression is as follows:

$$\boldsymbol{\theta}_{t} = \boldsymbol{\theta}_{t-1} - \alpha \frac{\mathbf{v}_{t}^{'}}{\sqrt{\mathbf{s}_{t}^{'} + \varepsilon}}$$
 (20)

where θ is the parameter of the update; α is the learning rate, which is set to 0.001 in this paper; $\epsilon=10^{-8}$ denotes a constant quantity that avoids a divisor of zero.

In this paper, we design to build a two-layer CNN model, the convolution kernel is set to 2×2 and the step size is set to 1. In order to prevent the loss of boundary information, the feature map is zero-padding, and the second layer is not filled. The specific parameters are shown in Table 2.

The model hyperparameters are determined using 10-fold cross-validation. Well A data is randomly split into ten pieces, nine of which are utilized for training and the remaining one for validation. The cycle is repeated ten times to guarantee that each randomly divided duplicate of the data acts as a validation set, and

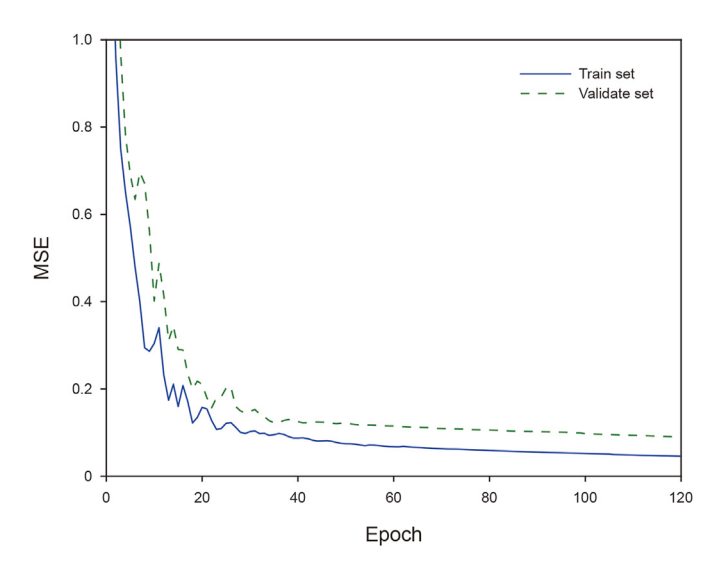


Fig. 8. The MSE trend of the CNN over different iterations.

the average results are used to evaluate the model's accuracy. The MSE is used to evaluate the model prediction ability, and Fig. 8 shows the MSE trend of the CNN over different iterations. It can be seen that the training error and the validation error are gradually stabilized after 60 iterations, and in order to prevent overfitting, the training is stopped after 60 iterations.

4.4. Application effectiveness

In order to verify the validity of the model, it is compared with the petrophysical model and the unconstrained 2D-CNN, respectively. The unconstrained 2D-CNN sets the petrophysical model's calculation results in both the training and test sets to zero, while

Table 2 The model parameter definitions.

Network layer	Number of convolution kernels/feature size	Convolution kernel size	Other parameters
Input	5 × 5	N/A	N/A
Conv1	32	2×2	Activate = "ReLU"
			Padding = "Valid"
Conv2	64	2×2	Activate = "ReLU"
			Padding = "Same"
GAP	64	N/A	N/A

Table 3The results of the test section of well A.

Model	Test section of well A	
	ρ	Relative error, %
Physically constrained 2D-CNN	0.98	2.14
Unconstrained 2D-CNN	0.90	3.61
Petrophysical model	0.92	6.14

maintaining the same number of iterations. The results of the test section of well A are shown in Table 3. The findings show that the Pearson correlation coefficient (ρ) and relative error of the prediction results of the physically constrained 2D-CNN with real values are 0.98, 2.14%, respectively. Compared with the unconstrained 2D-CNN and petrophysical model, the prediction results have the highest correlation and the lowest relative error. Fig. 9 shows a comparison of the three models' prediction effects on the test section of well A. It can be seen that the physically constrained 2D-CNN has the same trend as the petrophysical model and is more convergent compared to the unconstrained model. Although the

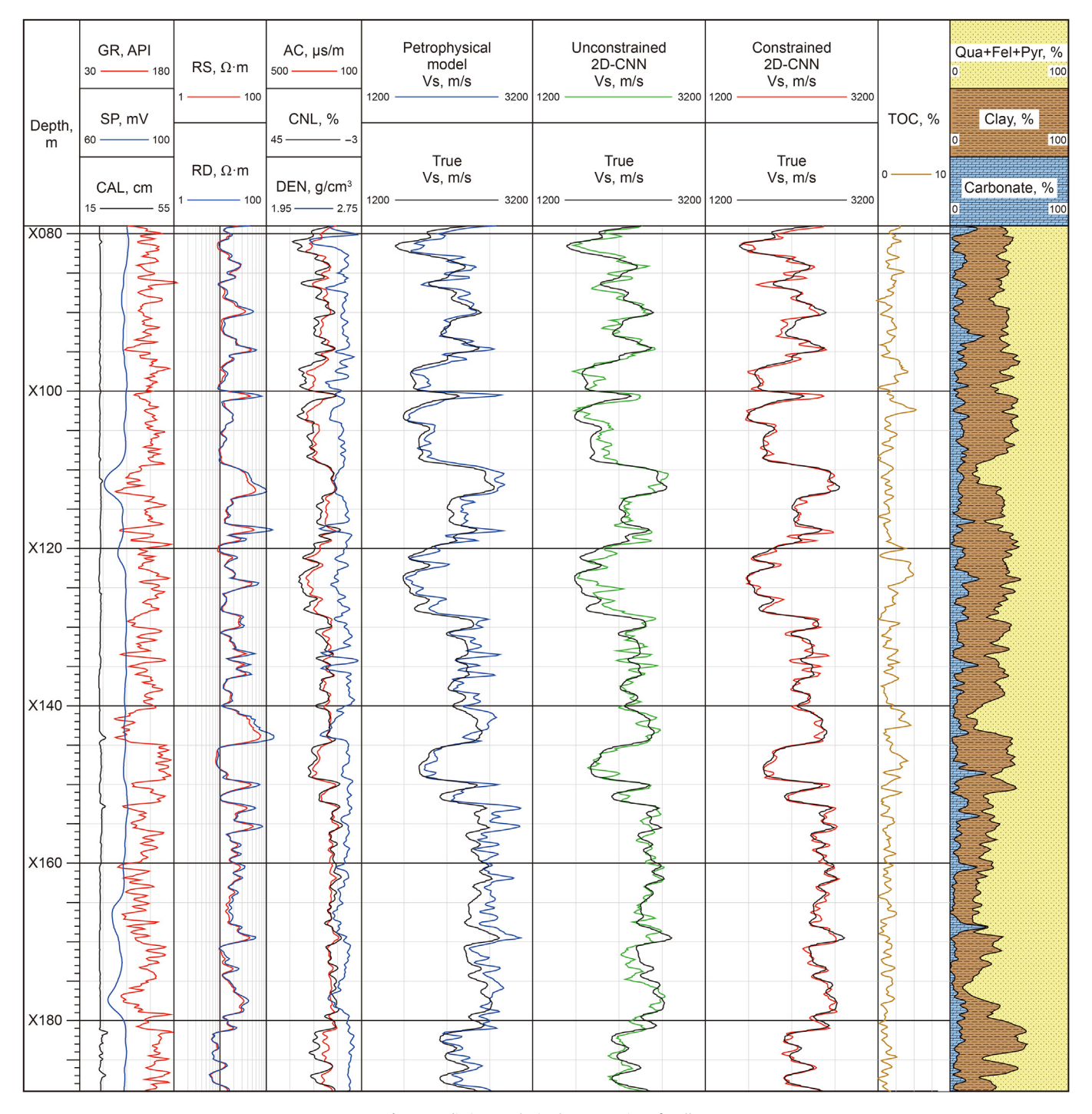


Fig. 9. Prediction results in the test section of well A.

Table 4The results of well B1.

Model	Well B1	
	ρ	Relative error, %
Physically constrained 2D-CNN	0.97	2.35
Unconstrained 2D-CNN	0.90	3.47
Petrophysical model	0.93	4.81

unconstrained model also obtained better results, there is a gap with the constrained model in the treatment of the inflection part of the curve and the trend of the curve change. Overall, the

physically constrained 2D-CNN's prediction results best match the actual S-wave velocity curves. The prediction results in this segment prove that the constrained model has a better ability to complement the S-wave velocity curve.

In order to verify the blind well prediction and generalization ability, well B1 and well B2 are predicted, respectively, with the training set unchanged. The prediction results for well B1 are shown in Table 4. The results show that the ρ and relative error of the prediction results of physically constrained 2D-CNN with the real values are 0.97 and 2.35%, respectively. The prediction accuracy is doubled compared to the petrophysical model. Although the relative error of the unconstrained model is lower than that of the petrophysical model, its correlation coefficient is low, which indicates the importance of the constraints of the petrophysical model. Fig. 10 shows a comparison of the three models' prediction

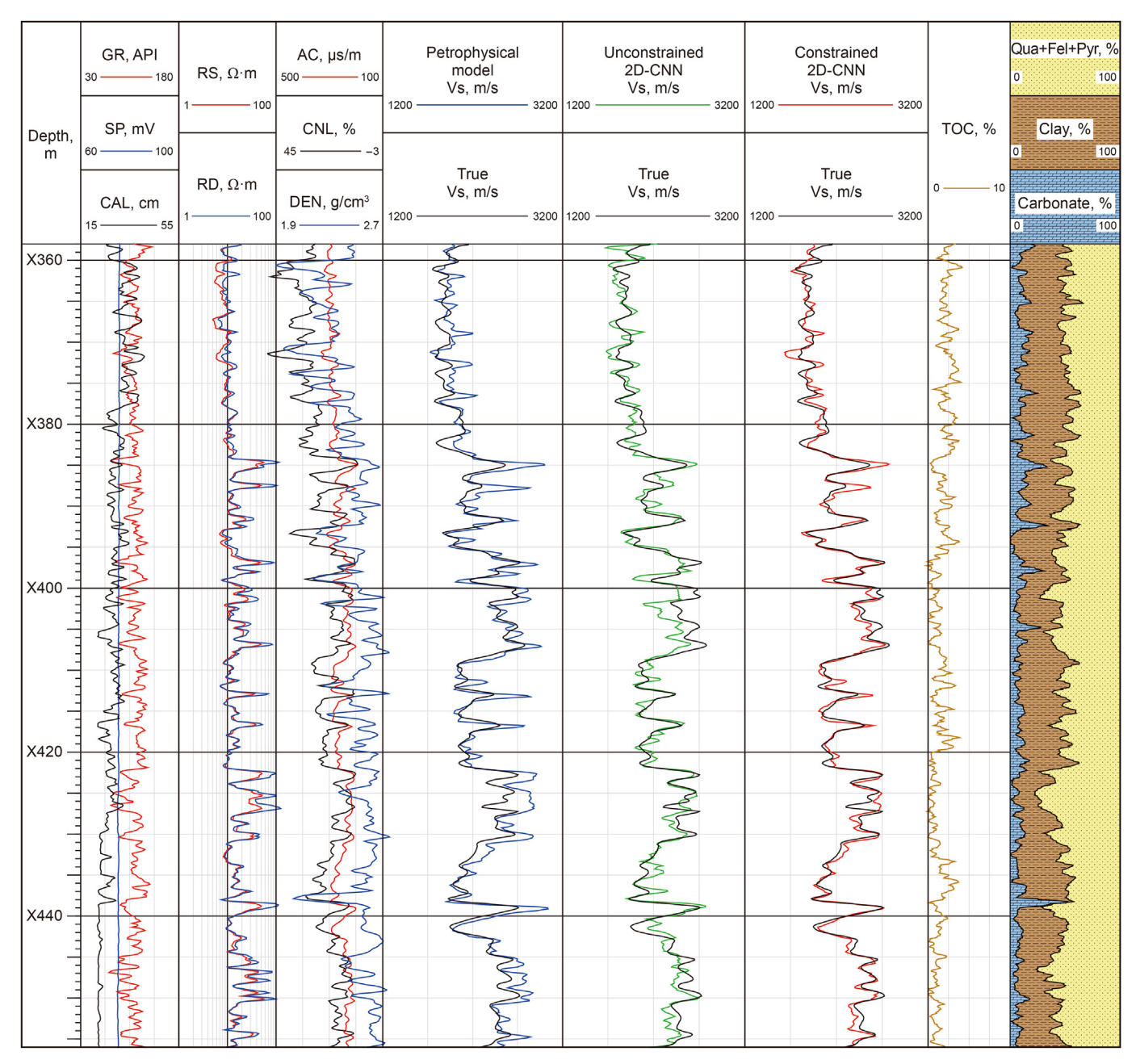


Fig. 10. Prediction results in the well B1.

Table 5 The results of well B2.

Model	Well B2	
	ρ	Relative error, %
Physically constrained 2D-CNN	0.96	2.89
Unconstrained 2D-CNN	0.91	4.45
Petrophysical model	0.93	6.26

effects for well B1. It can be seen at the peaks of the curves near X385 m and X439 m that the constrained model has a good correction ability at the extreme points compared with the petrophysical model. Meanwhile, the results of the unconstrained model are close to the real curves in these areas, which indicates that the remaining eight logs serve as corrections. The prediction results in this section prove that the constrained model has good blind well prediction accuracy.

The prediction results for well B2 are shown in Table 5. The results show that the ρ and relative error of the prediction results of physically constrained 2D-CNN with the real values are 0.96 and 2.89%, respectively, which is the best result among the three

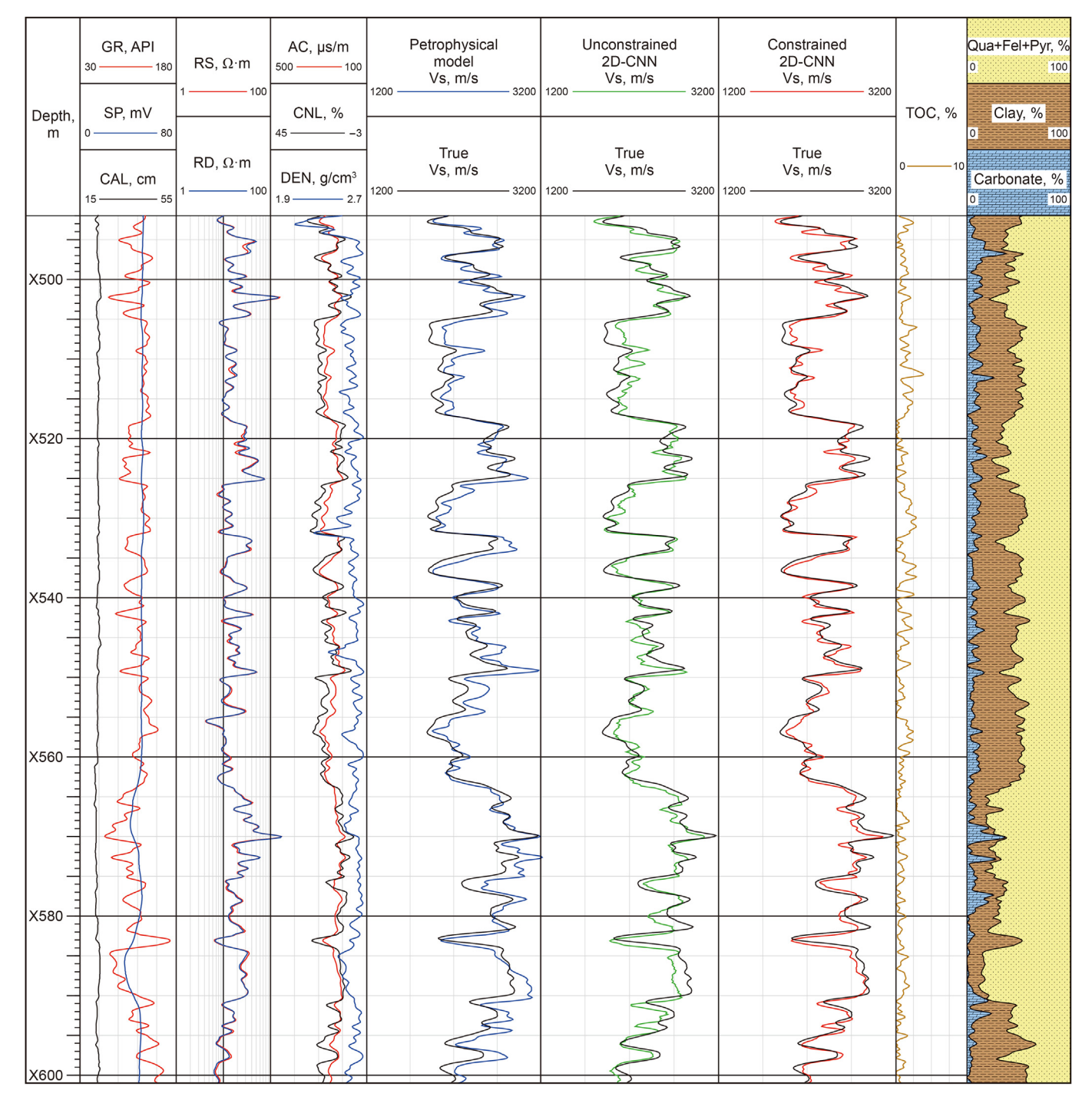


Fig. 11. Prediction results in the well B2.

models. Fig. 11 shows a comparison of the three models' prediction effects for the well B2. It can be seen that the petrophysical model results have a high similarity to the trend of the real curve, which in turn makes its correlation coefficient higher than the unconstrained model results. According to this phenomenon, it is further confirmed that the petrophysical model is necessary to constrain the 2D-CNN. The prediction results of this segment prove that the constrained model has good generalization ability.

From the prediction results, the physically constrained model's prediction of well B1 is better than the prediction of well B2. This is due to the closer distance between training well A and test well B1. So, in practical application, it is recommended to select typical wells in multiple areas of the study area to build a richer training set, and then the model will have stronger generalization ability and prediction accuracy.

We use box-plot to plot the relative errors of the different models in the three wells (Fig. 12). It can be more intuitively seen that the prediction results of the constrained model have the smallest average, median, and variance of the relative errors in the three test sections. Moreover, the shortest "box" indicates that the data distribution is more concentrated, which further proves that the prediction results of the constrained model are highly accurate and stable.

4.5. Evaluation of the GAP layer

To evaluate the impact of the GAP layer on the prediction results, we retrained a CNN + FC model for the constrained case using the same training set. In order to ensure the fairness and comparability

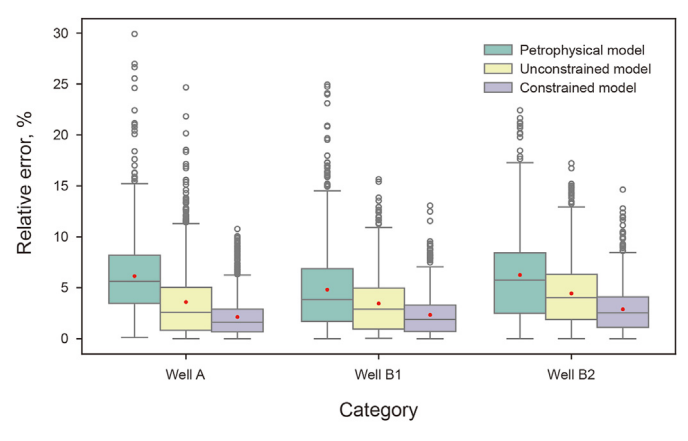


Fig. 12. Distribution of relative errors.

of the experiment, the FC layer is also set to 64 (consistent with the GAP size), keeping other network structures and parameter settings unchanged, and the results of the three wells are shown in Fig. 13.

The relative errors of CNN + FC in the three wells are 2.16%, 2.79% and 3.24%, respectively, which is a decrease in accuracy compared to CNN + GAP. Meanwhile, as far as generalization ability is concerned, CNN + FC performs worse than CNN + GAP, and it is preliminarily confirmed that the GAP layer outperforms the FC layer under the same parameter configuration. It is worth noting that the CNN + FC structure in this experiment adopts the same parameter configuration as that of the CNN + GAP, which is obtained by training the CNN + GAP. In addition, the FC layer is often used in conjunction with methods such as L_1 , L_2 regularization and dropout. We do not consider related optimization algorithms in this experiment.

4.6. Model explanation

(1) Figs. 14 and 15 show the CAMs of the 2D-CNN under constraints and without constraints, respectively. The CAMs show how much the model pays attention to different regions in the input feature map. The larger the value in the map, the more attention the model pays to the region. When V_s is used as the central position of the input feature map, the high-value area is concentrated in the center of the input feature map. It indicates that V_s plays an important influence on the prediction result at this time. When zero is used as the central position of the input feature map, the value of the middle region is small, indicating that zero has a small influence on the prediction result this time.

When using CAMs for classification problems, one can visualize the model's attention to the corresponding category in the graph by combining the generated CAMs with the input image. But there is still a lack of effective explainability methods when dealing with regression problems. Therefore, in order to further validate the influence of the petrophysical model on 2D-CNN, based on the S-wave velocity prediction study, this paper proposes the defined *C*-factor for the explainable results. The formula is as follows:

$$C_{i} = \frac{\sum_{x=1}^{N} p_{ix} \cdot g(m - \delta_{x})}{\sum_{x=1}^{N} g(m - \delta_{x})}$$

$$(21)$$

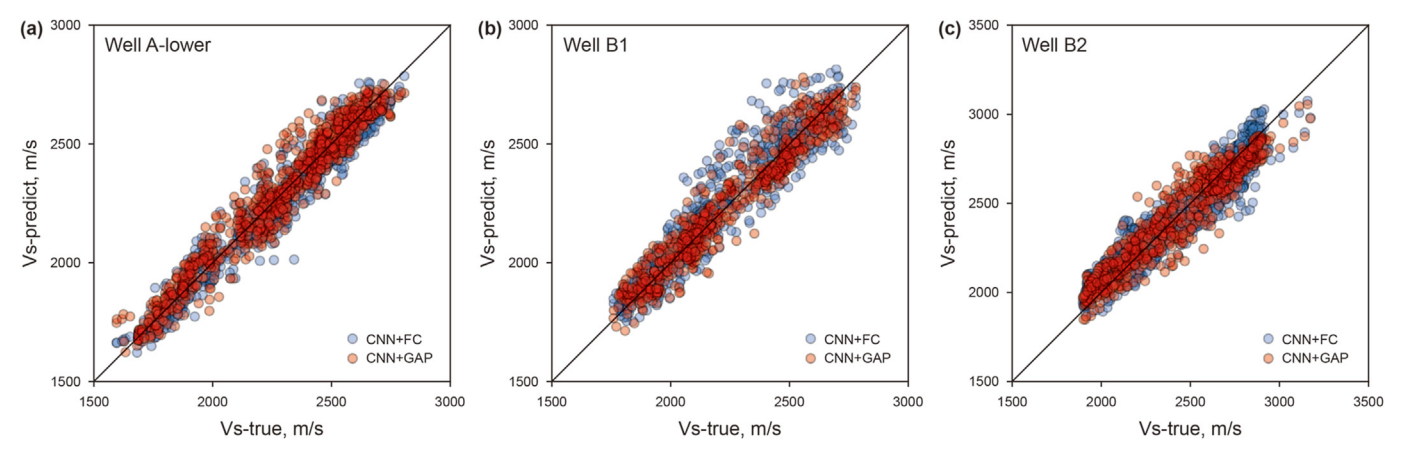


Fig. 13. Results for CNN + FC and CNN + GAP.

$$p_{ix} = \prod_{j=1, j \neq i}^{n} g(y_i - y_j)$$
 (22)

$$\delta_{\mathsf{X}} = \frac{|a_{\mathsf{X}t} - a_{\mathsf{X}p}|}{a_{\mathsf{X}t}} \times 100 \tag{23}$$

$$g(k) = \begin{cases} 0, k \le 0 \\ 1, k > 0 \end{cases}$$
 (24)

where C_i is used to evaluate the level of concern of the ith feature; N is the number of samples; g is the step function; m is the setting value relative error setting value; a_{xt} and a_{xp} are the measured and predicted S-wave velocities of the xth sample, respectively; δ_x is the calculated value of the relative error; p_{ix} is used to determine whether the ith feature of the xth sample is the maximum value in

the sample; y_i and y_j are the values of the ith feature and the jth feature in the CAMs, i cannot be equal to j; n is the number of sample features, which is 9 in this paper.

The C-factor at the central position of the input feature maps for the constrained and unconstrained models is calculated, and the results are shown in Fig. 16. The C-factor for the constrained model is higher than 30% overall, while the C-factor for the unconstrained model is lower than 10% overall, and even lower than 5% in Fig. 16(a)—(c). In addition, the C-factor of the constrained model has a decreasing trend with the increase in relative error. This indicates that V_S constrains the model results less as the error increases. Overall, the C-factor of the constrained model are significantly higher than those of the unconstrained model in the three test sections, indicating that the addition of the petrophysical model results to the input feature maps effectively improves the 2D-CNN's attention and realizes the constraints on the model.

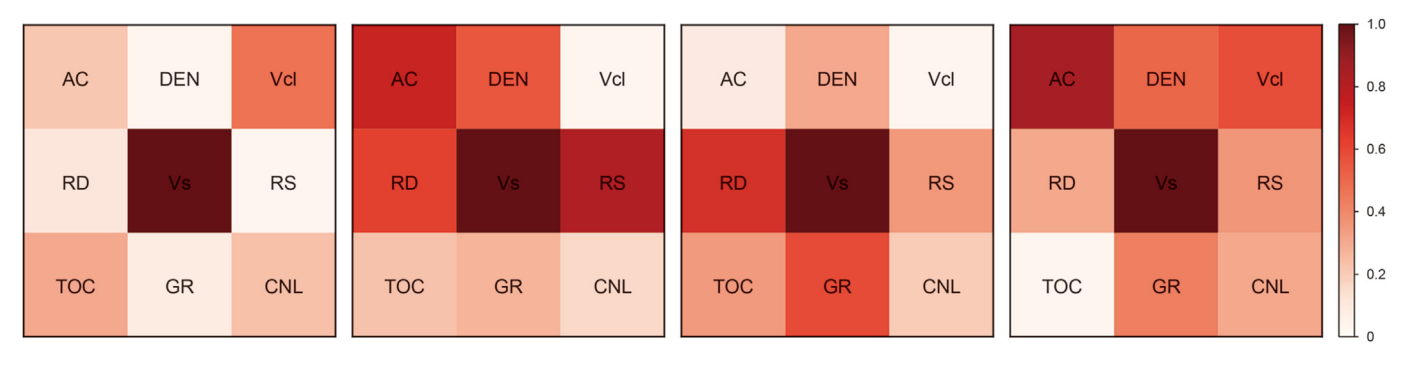


Fig. 14. Example of CAMs for the physically constrained model.

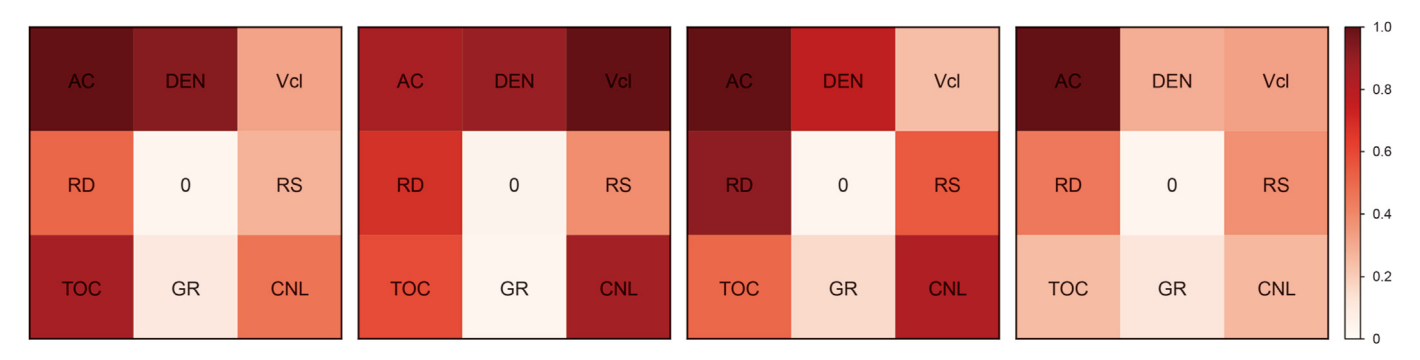


Fig. 15. Example of CAMs for the unconstrained model.

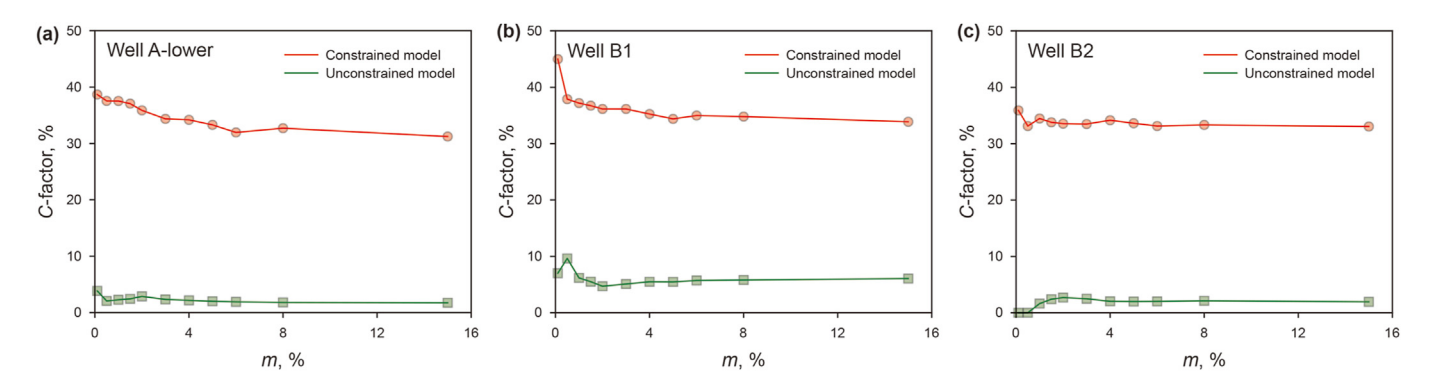
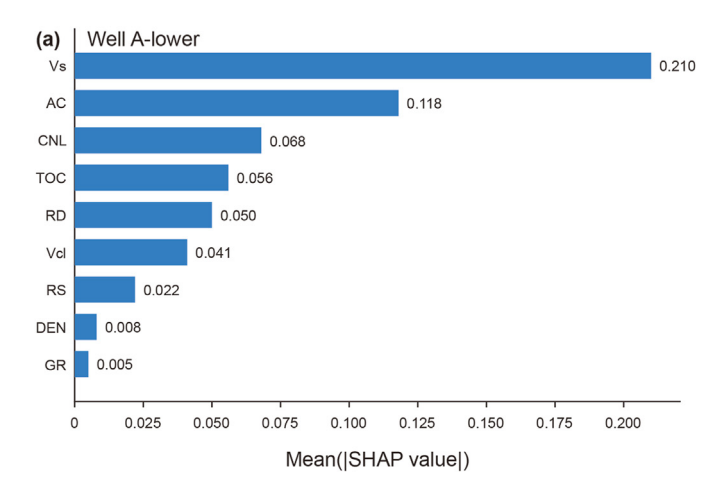
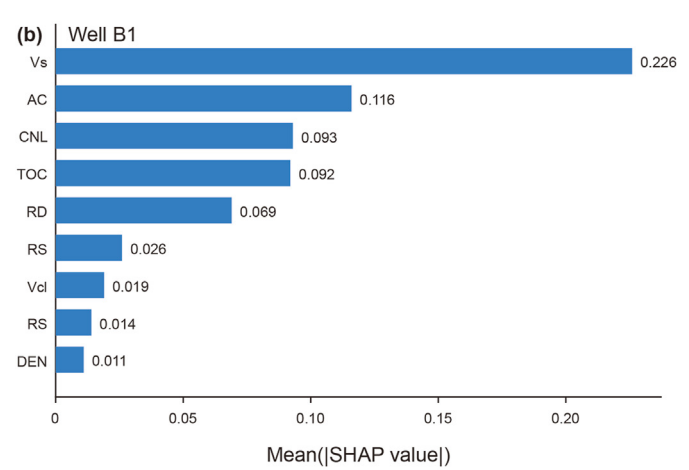


Fig. 16. Map of explainable results under physical constraints in three well sections.





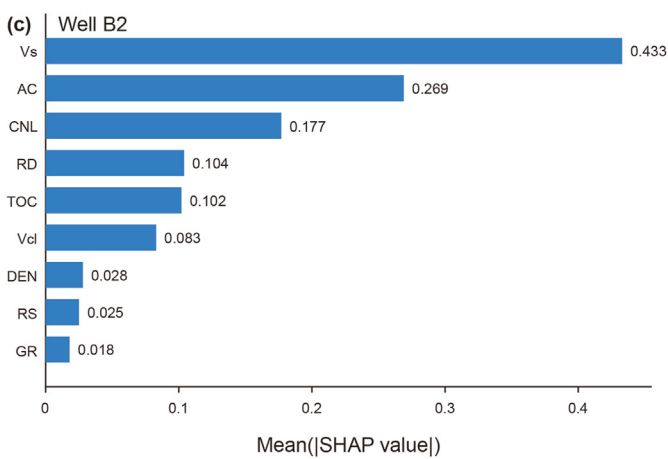


Fig. 17. SHAP results for Constrained 2D-CNN.

(2) We built a summary plot based on SHAP to assist in proving the importance of constraints (Chen et al., 2024). Fig. 17 illustrates a global feature importance plot for the three test sections, where each bar represents the average SHAP value of a feature. The magnitude of a feature's SHAP value indicates its contribution to the output of the model. A larger SHAP value indicates that the feature has a higher importance in the predictions of the model, and conversely, a smaller SHAP value indicates that it has a lower importance. As can be seen from the figure, the V_s has the greatest impact on the predicted results. This can assist in proving the importance of constraints. The next most significant influence on the predicted results is AC. This also shows that AC is

crucial for predicting the S-wave velocity. In addition, CNL, TOC, and RD also play an important role in the prediction.

It is worth noting that the SHAP is an explanation of the model predictions. When a machine learning model achieves high prediction accuracy, the relationship between features and predictions can be analyzed using SHAP. However, if the model's prediction accuracy is poor, the average SHAP value rankings of features become less significant.

5. Discussions

- (1) When the trained model is generalized to the study area, the blind wells are required to have the conventional eight logging data. However, when the blind wells lack logging data, a suitable model needs to be retrained. For new models lacking logging data, we still recommend using a 2D CNN, which can be achieved by assigning zero to some positions of the input feature map. This is because, on the one hand, 2D CNN can obtain more useful information, including feature information between petrophysics model and conventional logging data, as well as boundary information. On the other hand, 2D-CNN can effectively capture the local patterns and global relationships of the feature maps. It can extract important information about the spatial location by performing convolutional operations in the two dimensions of height and width. However, this requires a large number of experiments to obtain rigorous conclusions, which is also the focus of our subsequent work. In addition, it is worth noting that when retraining the model with less data, it should be ensured as much as possible that the conventional logging data used involves a variety of types, such as lithology curves, resistivity curves, and porosity curves.
- (2) The CNN has a strong dependence on training data. We believe that the more data involved in training, the more features can be extracted by CNN in the study area (Uchida et al., 2016; Luo et al., 2018; Xue et al., 2024). In particular, we replace the FC layer with a GAP layer, which reduces the risk of overfitting compared to traditional CNN. Since we have only three wells of measured data, the scale of the data used in this study is relatively small. In future research, we expect to perform S-wave prediction by accounting for more characteristics and including more training data sets. For example, if the data from all three wells are used as training samples, and then the trained model is applied to the study area for generalization, it is expected that better results can be achieved.
- (3) The petrophysics model in this manuscript did not consider the anisotropy and non-homogeneity of shale, but these phenomena cannot be ignored. In the subsequent work, if the data are available, there are two options to address the anisotropy and non-homogeneity of shale formations. One is to establish a more complex petrophysical model, which can fully consider the anisotropy and non-homogeneity, and then combine with the method proposed in this manuscript for prediction. The second is to calibrate the current results through experimental data, such as establishing a calibration chart.

6. Conclusions

In this paper, we propose a S-wave velocity prediction method in shale reservoirs based on explainable 2D-CNN under physical constraints. First, the high-sensitivity logging data related to S-

wave velocity are selected, then we establish a complex multimineral petrophysical model using mineral component analysis. Further, an explainable 2D-CNN based on macro-control of the petrophysical model is developed by combining single-channel 2D feature maps and GAP layer. The accuracy, generalizability, and validity of the physical constraints are verified through comparative experiments, CAM technique, defined *C*-factor, and SHAP model. The main conclusions and findings are as follows.

- (1) Based on the petrophysical properties of porous medium, the equivalent elastic modulus in the formation is obtained using the VRH boundary-averaged model. And then the S-wave velocity is obtained by calculating the Biot-Gassmann equation, which has a clear physical meaning. Although the Biot coefficient obtained from the AC data reduces the dispersion effect to some extent, there is still some error in shale reservoirs. The calculation accuracy needs to be improved. Based on the actual formation and data in the study area, the reader can establish a suitable petrophysical model and combine the method proposed in this paper to solve practical problems.
- (2) The results from the three test sections show that the constrained model has the highest ρ and the lowest relative errors compared to the unconstrained model and the petrophysical model. Although the relative error of the petrophysical model is the highest among the three models, the ρ is higher than the unconstrained model. This indicates that the constraints of the petrophysical model are critical. In addition, the prediction results of the test section in well A indicate that the model has a strong curve-completion ability; the prediction results of well B1 prove that the model has a high prediction accuracy in blind well prediction; and the prediction results of well B2 reflect that the model has a strong generalization ability. These results fully confirm the superiority of the method in S-wave velocity prediction and the necessity of physical constraints.
- (3) We use the CAM technique to highlight the regions of the input feature maps that the 2D-CNN focuses on. The results of the CAMs show that under the constraints, the high-value area is concentrated in the center of the input feature map. It indicates that the petrophysical model plays an important influence on the prediction result. Meanwhile, the *C*-factor is significantly higher under the constrained model than the unconstrained model, which further quantifies the impact of the petrophysical model on 2D-CNN. In addition, we establish the SHAP model and find that the petrophysical model has the highest average SHAP values across the three test wells, this serves as a supplementary demonstration of the importance of physical constraints in the modeling decision-making process.

CRediT authorship contribution statement

Zhi-Jun Li: Writing — original draft, Validation, Methodology, Conceptualization. **Shao-Gui Deng:** Writing — review & editing, Supervision, Resources. **Yu-Zhen Hong:** Validation, Formal analysis, Data curation. **Zhou-Tuo Wei:** Writing — review & editing, Data curation. **Lian-Yun Cai:** Visualization, Validation.

Declaration of competing interest

The authors declare that they have no known competing financial interests or personal relationships that could have appeared to influence the work reported in this paper.

Acknowledgement

This work is supported by the National Natural Science Foundation of China (Nos. 42374150, 42374152), Natural Science Foundation of Shandong Province (ZR2020MD050).

References

- Ali, M., Jiang, R., Ma, H.L., et al., 2021. Machine learning a novel approach of well logs similarity based on synchronization measures to predict shear sonic logs. J. Pet. Sci. Eng. 203, 108602. https://doi.org/10.1016/j.petrol.2021.108602.
- Azadpour, M., Saberi, M.R., Javaherian, A., et al., 2020. Rock physics model-based prediction of shear wave velocity utilizing machine learning technique for a carbonate reservoir, southwest Iran. J. Pet. Sci. Eng. 195, 107864. https://doi.org/10.1016/j.petrol.2020.107864.
- Bai, L.H., Liu, B., Du, Y.J., et al., 2022. Distribution characteristics and oil mobility thresholds in lacustrine shale reservoir: insights from N₂ adsorption experiments on samples prior to and following hydrocarbon extraction. Pet. Sci. 19 (2), 486–497. https://doi.org/10.1016/j.petsci.2021.10.018.
- Bai, Y., Tan, M.J., 2021. Dynamic committee machine with fuzzy-c-means clustering for total organic carbon content prediction from wireline logs. Comput. Geosci. 146, 104626. https://doi.org/10.1016/j.cageo.2020.104626.
- Castagna, J.P., Batzle, M.L., Eastwood, R.L., 1985. Relationships between compressional-wave and shear-wave velocities in clastic silicate rocks. Geophysics 50 (4), 571–581. https://doi.org/10.1190/1.1441933.
- Chen, J.Z., You, J.C., Wei, J.T., et al., 2024. Interpreting XGBoost predictions for shear-wave velocity using SHAP: insights into gas hydrate morphology and saturation. Fuel 364, 131145. https://doi.org/10.1016/j.fuel.2024.131145.
- Farouk, S., Sen, S., Ganguli, S.S., et al., 2021. Petrophysical assessment and permeability modeling utilizing core data and machine learning approaches a study from the Badr El Din-1 field, Egypt. Mar. Petrol. Geol. 133, 105265. https://doi.org/10.1016/j.marpetgeo.2021.105265.
- Han, D.H., Nur, A., Morgan, D., 1986. Effects of porosity and clay content on wave velocities in sandstones. Geophysics 51 (11), 2093–2107. https://doi.org/ 10.1190/1.1442062.
- Huang, H., Wang, T.F., Cheng, J.B., 2023. P/S-wave separation of multicomponent seismic data at the land surface based on deep learning. Geophysics 88 (3), V233–V247. https://doi.org/10.1190/geo2022-0282.1.
- Jiang, S.L., Zhou, Q.H., Li, Y.J., et al., 2023. Fracability evaluation of the middle—upper Permian marine shale reservoir in well HD1, western Hubei area. Sci. Rep. 13, 14319. https://doi.org/10.1038/s41598-023-40735-z.
- Khoshnoodkia, M., Mohseni, H., Rahmani, O., et al., 2011. TOC determination of Gadvan Formation in South Pars Gas field, using artificial intelligent systems and geochemical data. J. Pet. Sci. Eng. 78 (1), 119–130. https://doi.org/10.1016/ j.petrol.2011.05.010.
- Li, J.B., Wang, M., Lu, S.F., et al., 2020. A new method for predicting sweet spots of shale oil using conventional well logs. Mar. Petrol. Geol. 113, 104097. https:// doi.org/10.1016/j.marpetgeo.2019.104097.
- Li, Y., Wang, M., Yan, Y., et al., 2024. Paleoenvironment evolution and organic matter enrichment mechanisms in the first member of the Qingshankou Formation, Songliao Basin, China. Front. Earth Sci. 18, 364–383. https://doi.org/10.1007/ s11707-022-1067-1.
- Li, Y., Zhao, Q.M., Lyu, Q., et al., 2022. Evaluation technology and practice of continental shale oil development in China. Petrol. Explor. Dev. 49 (5), 1098–1109. https://doi.org/10.1016/S1876-3804(22)60335-5.
- Li, Z.J., Deng, S.G., Hong, Y.Z., et al., 2024. A novel hybrid CNN-SVM method for lithology identification in shale reservoirs based on logging measurements. J. Appl. Geophys. 223, 105346. https://doi.org/10.1016/j.jappgeo.2024.105346.
- Liu, B., Bai, L.H., Chi, Y.A., et al., 2019. Geochemical characterization and quantitative evaluation of shale oil reservoir by two-dimensional nuclear magnetic resonance and quantitative grain fluorescence on extract: a case study from the Qingshankou Formation in Southern Songliao Basin, northeast China. Mar. Petrol. Geol. 109, 561–573. https://doi.org/10.1016/j.marpetgeo.2019.06.046.
- Liu, G.Q., 2021. Challenges and countermeasures of log evaluation in unconventional petroleum exploration and development. Petrol. Explor. Dev. 48 (5), 1033–1047. https://doi.org/10.1016/S1876-3804(21)60089-7.
- Liu, Y.Y., Ma, X.H., Zhang, X.W., et al., 2021. A deep-learning-based prediction method of the estimated ultimate recovery (EUR) of shale gas wells. Pet. Sci. 18 (5), 1450–1464. https://doi.org/10.1016/j.petsci.2021.08.007.
- Liu, Z.S., Wang, K.N., Bao, Q.Z., et al., 2022. Prediction method of rock physics S-wave velocity in tight sandstone reservoir: a case study of Yanchang Formation in Ordos Basin. Acta Pet. Sin. 43 (9), 1284. https://doi.org/10.7623/syxb2022209007 (in Chinese).
- Luo, C., Li, X.J., Wang, L.T., et al., 2018. How does the data set affect CNN-based image classification performance?. In: 2018 5th International Conference on Systems and Informatics, pp. 361–366. https://doi.org/10.1109/ICSAI.2018.8599448.
- Passey, Q.R., Creaney, S., Kulla, J.B., et al., 1990. A practical model for organic richness from porosity and resistivity logs. AAPG (Am. Assoc. Pet. Geol.) Bull. 74 (12), 1777–1794. https://doi.org/10.1306/0C9B25C9-1710-11D7-8645000102C1865D.
- Pickett, G.R., 1963. Acoustic character logs and their applications in formation evaluation. J. Petrol. Technol. 15 (6), 659–667. https://doi.org/10.2118/452-PA.

- Selvaraju, R.R., Cogswell, M., Das, A., et al., 2017. Grad-CAM: visual explanations from deep networks via gradient-based localization. In: Proceedings of the IEEE International Conference on Computer Vision, pp. 618–626.
- Shao, C.R., Yin, X.Y., Zhang, F.M., et al., 2009. Shear wave velocity inversion with routine well logs based on rock physics and multi-mineral analysis. Earth Sci. 34 (4), 696–699 (in Chinese).
- Sohail, G.M., Hawkes, C.D., 2020. An evaluation of empirical and rock physics models to estimate shear wave velocity in a potential shale gas reservoir using wireline logs. J. Pet. Sci. Eng. 185, 106666. https://doi.org/10.1016/ j.petrol.2019.106666.
- Uchida, S., Ide, S., Iwana, B.K., et al., 2016. A further step to perfect accuracy by training CNN with larger data. In: 2016 15th International Conference on Frontiers in Handwriting Recognition, pp. 405–410. https://doi.org/10.1109/ICFHR 2016 0082
- Vernik, L., Castagna, J., Omovie, S.J., 2018. S-wave velocity prediction in unconventional shale reservoirs. Geophysics 83 (1), MR35—MR45. https://doi.org/10.1190/geo2017-0349.1.
- Wang, J., Cao, J.X., 2021. Data-driven S-wave velocity prediction method via a deeplearning-based deep convolutional gated recurrent unit fusion network. Geophysics 86 (6), M185—M196. https://doi.org/10.1190/geo2020-0886.1.
- Wang, J., Cao, J.X., Yuan, S., 2020. Shear wave velocity prediction based on adaptive particle swarm optimization optimized recurrent neural network. J. Pet. Sci. Eng. 194, 107466. https://doi.org/10.1016/j.petrol.2020.107466.
- Wang, J., Cao, J.X., Yuan, S., et al., 2022. Spatiotemporal synergistic ensemble deep learning method and its application to S-wave velocity prediction. Geosci. Rem. Sens. Lett. IEEE 19, 1–5. https://doi.org/10.1109/LGRS.2021.3123812.
- Wang, L., Liu, B., Bai, L.H., et al., 2023. Maceral evolution of lacustrine shale and its effects on the development of organic pores during low mature to high mature stage: a case study from the Qingshankou Formation in northern Songliao Basin, northeast China. Pet. Sci. 20 (5), 2709–2725. https://doi.org/10.1016/j.petsci.2023.08.025.
- Xu, S., White, R.E., 1995. A new velocity model for clay-sand mixtures. Geophys. Prospect. 43 (1), 91–118. https://doi.org/10.1111/j.1365-2478.1995.tb00126.x.
- Xu, Z.H., Li, J.T., Li, J., et al., 2024. Application of 9-component S-wave 3D seismic data to study sedimentary facies and reservoirs in a biogas-bearing area: a case study on the Pleistocene Qigequan Formation in Taidong area, Sanhu Depression, Qaidam Basin, NW China. Petrol. Explor. Dev. 51 (3), 647–660. https:// doi.org/10.1016/S1876-3804(24)60494-5.
- Xue, L., Xu, S., Nie, J., et al., 2024. An efficient data-driven global sensitivity analysis method of shale gas production through convolutional neural network. Pet. Sci. 21 (4), 2475–2484. https://doi.org/10.1016/j.petsci.2024.02.010.
- Yang, B.C., Xue, L., Duan, Y.T., et al., 2021. Correlation study between fracability and brittleness of shale-gas reservoir. Geomech. Geophys. Geo-energ. Geo-resour. 7, 31. https://doi.org/10.1007/s40948-021-00231-y.
- Yang, L.X., Sun, S.Z., Ji, L.L., 2019. S-Wave Velocity Prediction for Complex Reservoirs Using a Deep Learning Method. SEG Technical Program Expanded Abstracts, pp. 2574–2578. https://doi.org/10.1190/segam2019-3216200.1.
- Yasin, Q., Sohail, G.M., Liu, K.Y., et al., 2021. Study on brittleness templates for shale gas reservoirs-A case study of Longmaxi shale in Sichuan Basin, southern China. Pet. Sci. 18 (5), 1370–1389. https://doi.org/10.1016/j.petsci.2021.09.030.
- Ye, Y.P., Tang, S.H., Xi, Z.D., et al., 2022. A new method to predict brittleness index for shale gas reservoirs: insights from well logging data. J. Pet. Sci. Eng. 208, 109431. https://doi.org/10.1016/j.petrol.2021.109431.

- Yi, D., Ahn, J., Ji, S., 2020. An effective optimization method for machine learning based on ADAM. Appl. Sci. 10 (3), 1073. https://doi.org/10.3390/app10031073.
- Yildirim, O., Talo, M., Ay, B., et al., 2019. Automated detection of diabetic subject using pre-trained 2D-CNN models with frequency spectrum images extracted from heart rate signals. Comput. Biol. Med. 113, 103387. https://doi.org/10.1016/ j.compbiomed.2019.103387.
- Yin, X.Y., Liu, Q., 2016. Anisotropic rock physics modeling of tightsandstone and applications. Journal of China University of Petroleum (Edition of Natural Science) 40 (2), 52–58 (in Chinese).
- Yin, X.Y., Liu, X.X., Cao, D.P., 2013. Elastic parameters calculation for tight sand reservoir based on Biot-consistent theory. Geophys. Prospect. Pet. 52 (5), 445–451 (in Chinese).
- You, J.C., Zhao, J.Q., Huang, X.G., et al., 2023. Explainable convolutional neural networks driven knowledge mining for seismic facies classification. IEEE Trans. Geosci. Rem. Sens. 61, 1–18. https://doi.org/10.1109/TGRS.2023.3280364.
- Yu, B., Zhou, H., Huang, H.D., et al., 2020. A modified shear-wave velocity estimation method based on well-log data. J. Appl. Geophys. 173, 103932. https://doi.org/ 10.1016/j.jappgeo.2019.103932.
- Zhang, B., Jin, S.G., Liu, C., et al., 2020. Prediction of shear wave velocity based on a statistical rock-physics model and Bayesian theory. J. Pet. Sci. Eng. 195, 107710. https://doi.org/10.1016/j.petrol.2020.107710.
- Zhang, F.J., Deng, S.G., Wang, S.L., et al., 2022. Convolutional neural network long short-term memory deep learning model for sonic well log generation for brittleness evaluation. Interpretation 10 (2), T367–T378. https://doi.org/ 10.1190/INT-2021-0103.1.
- Zhang, J.F., Xu, X.Y., Bai, J., et al., 2020. Enrichment and exploration of deep lacustrine shale oil in the first member of Cretaceous Qingshankou Formation, southern Songliao Basin, NE China. Petrol. Explor. Dev. 47 (4), 683–698. https://doi.org/10.1016/S1876-3804(20)60085-4.
- Zhang, J.Y., Zhu, R.K., Wu, S.T., et al., 2023. Microscopic oil occurrence in high-maturity lacustrine shales: Qingshankou Formation, Gulong Sag, Songliao Basin. Pet. Sci. 20 (5), 2726–2746. https://doi.org/10.1016/j.petsci.2023.08.026.
- Zhang, K., Li, H.Y., Wang, X.J., et al., 2020. Retrieval of shallow S-wave profiles from seismic reflection surveying and traffic-induced noise. Geophysics 85 (6), EN105—EN117. https://doi.org/10.1190/geo2019-0845.1.
- Zhang, Y., Zhang, C.L., Ma, Q.Y., et al., 2022. Automatic prediction of shear wave velocity using convolutional neural networks for different reservoirs in Ordos Basin. J. Pet. Sci. Eng. 208, 109252. https://doi.org/10.1016/j.petrol.2021.109252.
- Zhang, Y., Zhong, H.R., Wu, Z.Y., et al., 2020. Improvement of petrophysical work-flow for shear wave velocity prediction based on machine learning methods for complex carbonate reservoirs. J. Pet. Sci. Eng. 192, 107234. https://doi.org/10.1016/j.petrol.2020.107234.
- Zhao, J.F., Mao, X., Chen, L.J., 2019. Speech emotion recognition using deep 1D & 2D CNN LSTM networks. Biomed. Signal Process Control 47, 312–323. https://doi.org/10.1016/j.bspc.2018.08.035.
- Zhao, Z.P., Li, Q.F., Zhang, Z.X., et al., 2021. Combining a parallel 2D CNN with a self-attention Dilated Residual Network for CTC-based discrete speech emotion recognition. Neural Netw. 141, 52–60. https://doi.org/10.1016/j.neunet.2021.03.013.
- Zhou, B.L., Khosla, A., Lapedriza, A., et al., 2016. Learning deep features for discriminative localization. In: Proceedings of the IEEE Conference on Computer Vision and Pattern Recognition, pp. 2921–2929.